SILICON/SILICON-GERMANIUM QUANTUM DOTS WITH SINGLE-ELECTRON TRANSISTOR CHARGE SENSORS

A Thesis

Submitted to the Faculty

in partial fulfillment of the requirements for the

degree of

Doctor of Philosophy

in

Physics and Astronomy

by

Mingyun Yuan

DARTMOUTH COLLEGE

Hanover, New Hampshire

May 6, 2013

Examining Committee:

A. J. Rimberg, Chair

M. P. Blencowe

L. Viola

M. A. Eriksson

F. Jon Kull, Ph.D.
Dean of Graduate Studies

Abstract

Si/SiGe quantum dots (QDs) are promising candidates for spin-based quantum bits (qubits) as a result of the reduced spin-orbit coupling as well as the Si isotopes with zero nuclear spin. Meanwhile, qubit readout is a challenge related to semiconductor-based quantum computation. A superconducting single-electron transistor (SET), when operating in the radio-frequency (rf) regime, has a combination of high charge sensitivity and low back-action and can potentially become an ideal charge sensor for the QDs.

This thesis describes the development of superconducting SET charge sensors for Si/SiGe QDs. Using rf-SETs we have detected real-time electron tunneling events on the order of 10 microseconds in a single QD and mapped out the stability diagram of a double QD, showing spin blockade and bias triangles due to excited-state transitions. In Addition, Kondo effects that are significantly different from the standard spin 1/2 model have been observed and investigated in both perpendicular and in-plane magnetic fields, indicating the interplay between the spin and valley degrees of freedom in Si.

Acknowledgements

When I first entered graduate school, we were told that this would be a journey to transform ourselves from students to experts. The truth is, as years go by, I increasingly realize how little I actually know. I may not have become an expert but I did gain knowledge about a lot of things whose existence I was not even aware of. This would not have been possible without the help and guidance of many colleagues and friends.

I would first like to thank my advisor Prof. Alex Rimberg, who allowed me the freedom to explore the experiments at my own pace while providing me with guidance whenever needed. I learned from Alex practical skills on eliminating ground loops, radio-frequency measurement and scientific writing, etc.. What is more important, he taught me that intuition about experiments can be refined and being a young woman is not an excuse for avoiding any technical problems, which have a greater impact on my academic vision.

My fellow graduate students and the postdoc researchers made the experience in the lab more than pleasant. I am grateful to Feng Pan and Tim Gilheart for introducing me to the area of micro fabrication and research on Si/SiGe as well as their pioneering effort in developing the recipe for low-leakage gates. I have been fortunate to work in an amazing lab furnished and maintained by Zhongqing Ji,

Mustafa Bal, Feng Pan and Juliang Li. I could not imagine where to start without the sophisticated apparatus readily built by my various labmates. Joel Stettenheim gave me tremendous help in the operation of the dilution refrigerators and was always ready to lend a hand when troubles occured. Zhen Yang and Chunyang Tang, with whom I worked closely, were instrumental in the Si/SiGe project and the daily running of the experiments. Zhen's ability to fabricate highly reliable devices ensured good results and I benefited much from Chunyang's profound understandings of physical concepts. I would also like to thank Fei Chen who shared numerous tips and ideas with me during the five years we spent together in the lab.

I have always enjoyed conversations with Prof. Miles Blencowe, physics related or otherwise. Miles illuminated the area of superconducting devices for me and really counts as half an advisor.

Finally, I would like to thank my parents and my husband Ralf for their unconditional support and tolerance. They are everything I could ever wish for in a happy family.

Contents

List of Figures

List of Tables

Chapter 1

Introduction

1.1 Quantum computing

The pioneering ideas in quantum computing date back to the 1980s. In 1982 Richard Feynman suggested that building a computer based on the principles of quantum mechanics would eliminate the intrinsic difficulties in simulating quantum mechanical systems with a classical computer [1]. In 1985 David Deutsch started to consider computing devices based upon the principles of quantum mechanics. He also demonstrated that quantum computers have the power to solve certain computational problems inaccessible to a classical computer [2]. This idea was developed further in the 1990s. Peter Shor demonstrated that a quantum computer has the ability to solve two problems of great importance, namely the problem of finding the prime factors of an integer, and the discrete logarithm problem [3]. Lov Grover proved that a quantum computer can dramatically speed up the process of searching through an unsorted database [4].

1.1 Quantum computing

A classical bit can only occupy either '0' or '1' at any time, while a quantum bit (qubit) can be the superposition of both states, $x|0\rangle + y|1\rangle$, with probabilities $|x|^2$ and $|y|^2$ for $|0\rangle$ and $|1\rangle$, respectively. An n-qubit system would therefore be the superposition of 2^n states, which enables a single operation to be performed on multiple input combinations simultaneously.

Loss and DiVincenzo proposed an implementation of a universal set of gates for quantum computing using the spin states of coupled single-electron quantum dots [5]. Qubits in semiconductors are promising for the scale-up of future quantum circuits. Si in particular has long coherence time due to the existence of zero-nuclear spin isotopes. Being the second most abundant material on earth, Si is a favorable economic choice. Last but not least, the current semiconductor industry is largely based on Si. Most of the available technology and engineering can potentially be transferred directly to quantum circuits.

In quantum computation there are two important timescales generally referred to as T_1 and T_2, in analogy to the spin-lattice relaxation time T_1 and the spin-spin relaxation time T_2 in nuclear magnetic resonance (NMR) systems. In a qubit T_1 is the spin energy relaxation time, governing the mechanism by which the qubit returns to equilibrium with the environment while T_2 is the dephasing time after which the phase information in the qubit is lost due to spin precession. In Ref. [6] the effects of T_1 and T_2 are explained in terms of the transformation of the density matrix,

$$\begin{pmatrix} a & b \\ b^* & 1-a \end{pmatrix} \rightarrow \begin{pmatrix} (a-a_0)e^{-t/T_1}+a_0 & be^{-t/T_2} \\ b^*e^{-t/T_2} & (a-a_0)e^{-t/T_1}+1-a_0 \end{pmatrix}. \qquad (1.1)$$

For $t > T_2$, the phase information stored in the off-diagonal terms is erased.

Meanwhile, for $t > T_1$ the energy relaxes to the thermal equilibrium characterized by a_0. Eventually the qubit collapses to the basis states of the environment,

$$\begin{pmatrix} a_0 & 0 \\ 0 & 1-a_0 \end{pmatrix}. \tag{1.2}$$

In practice, instead of T_2, it is usually the time-ensemble-averaged dephasing time T_2^* that is measured.

1.2 Si/SiGe heterostructures

In recent years, considerable progress has been achieved on Si-based quantum dots (QDs) [7, 8, 9, 10, 11, 12]. A prominent motivation is that the reduced spin-orbit coupling as well as the zero nuclear spin in ^{28}Si and ^{30}Si, which together make up 95% of the natural-abundance of silicon, give rise to unusually long electron spin coherence times [13, 14]. On the other hand, as the more mature material in study of transport in nanostructures, GaAs does not have isotopes without nuclear spin, and the presence of nuclear spins eventually contributes to spin decoherence [15, 16]. These properties make Si-based quantum devices, including Si/SiGe QDs, promising candidates for spin-based qubits, which are a potential platform for quantum information processing [17, 18]. Recent measurements have found the spin relaxation time T_1 to be as long as $\sim$6 s at a field of 1.5 T for phosphorus donors in Si [19], and $\sim$3 s at a field of 1.85 T in Si/SiGe QDs [20]. Lifetime of triplet states in a Si/SiGe double QD (DQD) have been measured to be $\sim$10 ms in the absence of magnetic field and can reach 3 s at 1 T [21]. In an undoped Si/SiGe DQD, a nuclear-induced dephasing time $T_2^* = 360$ ns

Table 1.1: Relaxation times in GaAs and Si/SiGe QDs

QD	T_1	T_2^*
GaAs	0.85 ms at 8 T, single spin [24] 70 μs, singlet-triplet (S-T) [27]	10 ns, single spin [25]; 37 ns, S-T [26] 200 μs, S-T with CPMG echo[23]
Si/SiGe	3 s at 1.85 T, single spin [20] 3 s at 1 T, S-T[21]	360 ns [22]

has been reported [22]. Table 1.1 is a brief summary of the measured T_1 and T_2^* in GaAs and Si/SiGe QDs. The most extraordinary result among them is probably the dephasing time in GaAs qubit exceeding 200 μs with Carr-Purcell-Meiboom-Gill (CPMG) echo sequence [23].

Although Si/SiGe QDs has many desirable features compared to GaAs/AlGaAs QDs, significant challenges are present. The most crucial issue that needs to be resolved is the leakage current associated with smaller Schottky barriers. Defects in the material are hard to avoid due to the strain that occurs in the growth of the heterostructure. The effective mass of Si, being almost 3 times larger than that in GaAs, results in a smaller energy level spacing in the QD so the geometric dimensions of the devices have to be smaller. The presence of a valley degeneracy further complicates the matter, but can also lead to the observation of interesting physics.

The development of Si/SiGe heterostructure, which has enabled band structure engineering in this materials system, has opened up the possibility of realizing silicon-based qubits and allows new physics to be explored [28, 29, 30]. Compared to GaAs, in which bandgap engineering was originally pioneered, Si/SiGe heterostructure devices took much longer to develop due to the more demanding growth technology as well

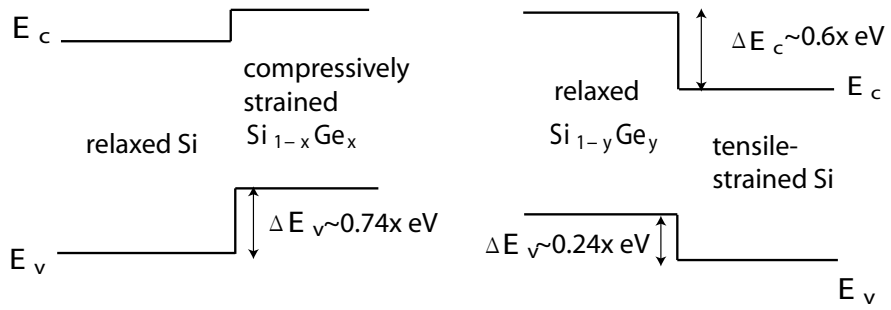

Figure 1.1: Band structures for compressively strained $Si_{1-x}Ge_x$ on relaxed Si and tensile-strained Si on relaxed $Si_{1-y}Ge_y$

as issues related to strain. The near-perfect lattice match between GaAs and AlGsAs results in high quality wafers. In contrast, the lattice constant of germanium is 4.2% larger than that of silicon. Consider the case in which a thin $Si_{1-x}Ge_x$ film is grown on top of a $Si_{1-y}Ge_y$ film. The top layer is compressively strained for $x > y$ while tensile strained for $x < y$. As shown in Fig. 1.1, to produce a quantum well with a large enough discontinuity to confine electrons, a tensile-strained Si or $Si_{1-x}Ge_x$ layer must be grown on a relaxed $Si_{1-y}Ge_y$ substrate, where $x < y$ [31]. The tensile-strained layer and the substrate have different conduction band minima. An electron gas is formed at their interface as a result. The electrons are bound to the interface, free to move in the plane parallel to the interface, hence the name 'two dimensional electron gas' (2DEG).

The Si/SiGe heterostructure wafers are provided by our collaborators at the University of Wisconsin, who have first observed Coulomb blockade in Si/SiGe [32] and later performed charge sensing in a Si/SiGe double QD with a quantum point contact

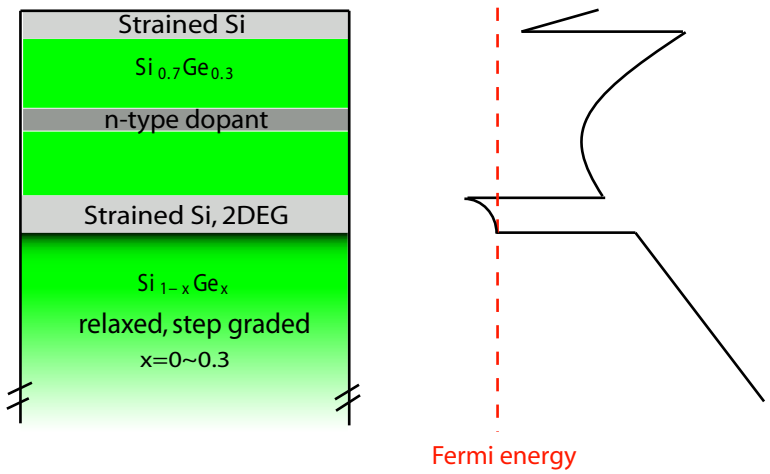

Figure 1.2: Schematic diagram of Si/SiGe heterostructure and bandgap structure

(QPC) charge sensor [33]. Fig. 1.2 illustrates the schematic of a Si/SiGe heterostructure and conduction band alignment.

The Si/SiGe heterostructure is grown using chemical vapor deposition (CVD). A step-graded virtual substrate is grown on Si (001) that was miscut 2 degrees towards (010). A 1 μm thick $Si_{0.7}Ge_{0.3}$ buffer layer is deposited next, followed by an 18 nm Si well where the two-dimensional electron gas (2DEG) is located. A 22 nm intrinsic layer, a 1 nm doped layer ($\sim 10^{-19}$ cm^{-3} phosphorous), a second intrinsic alloy layer of $\sim$ 50 to 76 nm, and finally a 9 nm Si cap layer are grown subsequently.

1.3 Fast charge read-out

A challenging task related to semiconductor-based quantum computation is qubit readout [17, 34]. The quantum point contact (QPC) is the most commonly used readout device thanks to its simple fabrication process [35, 24, 25]. Silicon QDs themselves have also been used as charge sensors [36]. However, unwanted dissipation in a QPC or QD is inevitable, since the charge carriers are normal electrons. A superconducting single-electron transistor (SET), on the other hand, has carriers of quasi-particles and Cooper pairs allowing for reduced dissipation and better sensitivity. Fast charge readout can be performed with the radio frequency SET (rf-SET) [37], as has been demonstrated in GaAs-based QDs [38]. Excellent sensitivity (on the order of $10^{-6}\ e/\sqrt{\text{Hz}}$) [38, 39] combined with low back-action [40] has been reported for the rf-SET.

1.4 Structure of this thesis

This thesis comprises mainly two parts. The former is the effort to form controllable QDs in Si/SiGe and the study of their transport properties. The latter is to incorporate SET charge sensors to perform both dc and rf charge readout of the QDs.

Chapter 1 is a brief overview of quantum computing as well as the motivation for developing Si/SiGe QDs and the rf-SET charge sensors. **Chapter 2** introduces the fabrication process, with an emphasis on the low-leakage Schottky gates, and the cryogenic refrigerators for low-temperature measurement. **Chapter 3** presents the experimental results of single QD measurements, demonstrating Coulomb blockade. When performing transport measurement we observe interesting Kondo effect related

to the valley degree of freedom unique to Si, which is discussed in **Chapter 4**. The following four chapters focus on SET charge sensing. **Chapter 5** introduces the superconducting SET and the dc charge sensing of the QD is demonstrated. **Chapter 6** moves forward to the rf regime and explains in detail the method of rf-SET with real-time charge sensing data. **Chapter 7** presents experimental data and detailed analysis of double QD (DQD) charge sensing with rf-SET. Spin blockade as well as bias triangles due to transition through excited states are observed. To conclude, in **Chapter 7** the future direction will be indicated.

Chapter 2

Device fabrication and cryogenics

2.1 Fabrication of Si/SiGe quantum dots with low-leakage gates

Considering the complexity of the QD-SET system, it is essential to develop a reliable fabrication process that guarantees a high yield of successful devices. The most basic fabrication technique involves patterning with photolithography / electron beam lithography, and the subsequent deposition of metals. Photolithography is used for pattern features larger than a micron including the etch pattern, ohmic contacts and photo gates. A layered Au/Sb/Au film is evaporated to form the ohmic contacts, which typically yields a resistance of tens of kiloohms after annealing at 400°C in a gas mixture of H_2 and He (20% H_2). Pd is evaporated in an electron beam evaporator to form the Schottky gates. Fig. 2.1 shows the device after the photolithography steps are completed.

Leakage currents in Si/SiGe devices can become significant, preventing the forma-

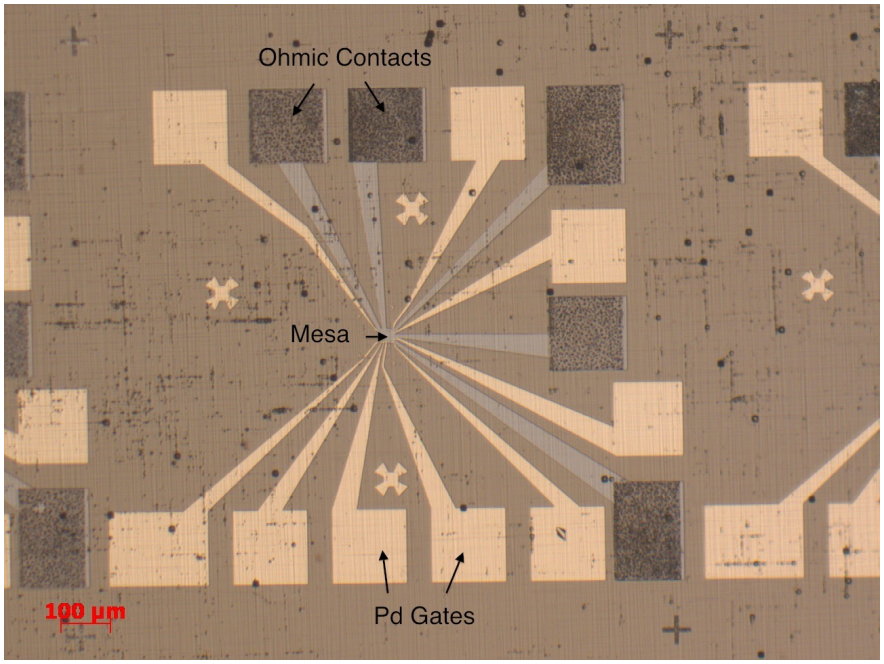

Figure 2.1: Optical micrograph of a device in Si/SiGe

tion of stable QDs. A combination of deep etch and oxide backfill is used to reduce the leakage current. We use a CF_4/O_2 plasma in a reactive ion etcher (RIE) to remove the majority of the surface, leaving only the mesa where the QD is formed and the ohmic-contact leads. We then immediately back-fill the etched area with AlO_x in an electron beam (e-beam) evaporator before resist removal, as illustrated by Fig. 2.2. (If possible, atomic layer deposition (ALD) would be more desirable.) The etch depth is typically 50 nm beyond the estimated depth of the 2DEG. After an additional patterning step, layered AlO_x/Ti/Pd is deposited to form the Schottky gates in the e-beam evaporator. Before gate evaporation we return the sample to the RIE and use CF_4 (without O_2) to remove the native oxide. Neither the sample surface nor the AlO_x backfill is damaged with this dry etch.

The QD is patterned subsequently with e-beam lithography. After the removal of

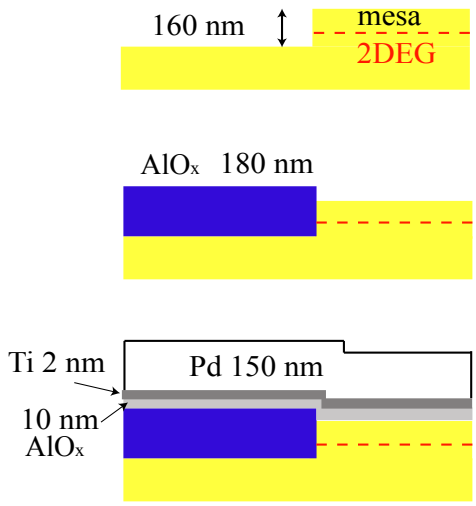

Figure 2.2: Sequence of gate fabrication steps

oxide with CF_4, Pd is deposited directly on the mesa to form the dot gates, which are extensions of the photolithographic Pd gates. Fig. 2.3 shows a scanning electron micrograph of a completed QD on a mesa.

To detect the leakage, voltage is applied on each gate and any resulting current is measured through an ohmic contact. Our gate fabrication techniques significantly suppress leakage currents. The Pd gates show no signs of leakage within the sensitivity of our measurement (∼picoampere) up to an applied voltage of -3 to -5 V, as shown in Fig. 2.4 where curves of different colors correspond to different gates.

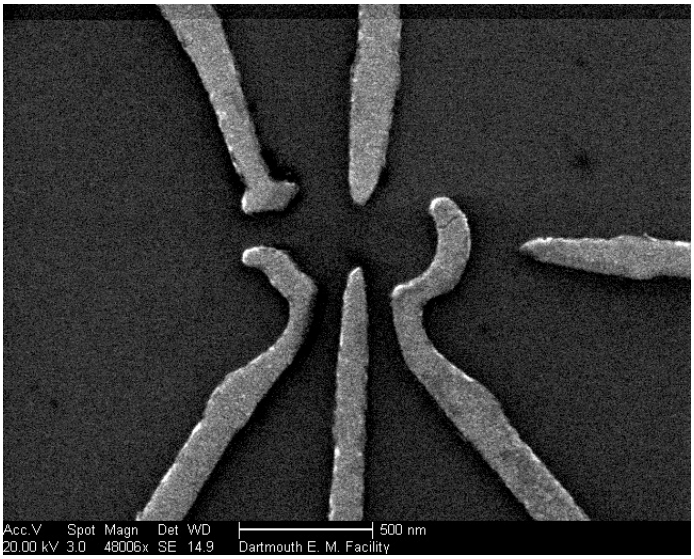

Figure 2.3: SEM image of a QD defined by Pd gates

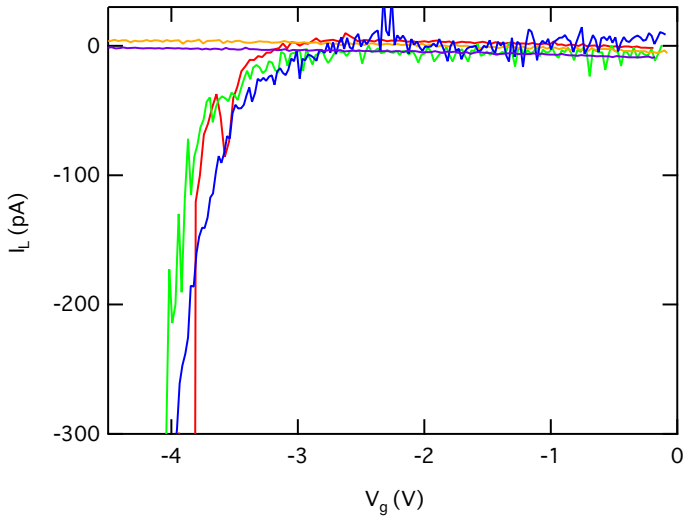

Figure 2.4: Leakage currents vs. gate voltage for a device with low-leakage Schottky gates

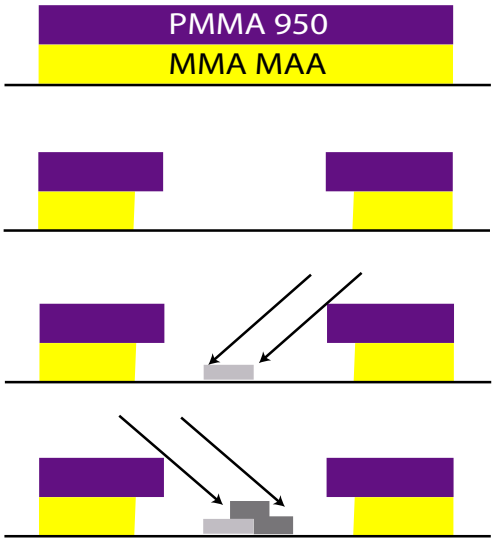

Figure 2.5: Sequence of SET shadow evaporation

2.2 Fabrication of Al single-electron transistor

The Al SET is fabricated with shadow evaporation as illustrated in Fig. 2.5. The substrate is first coated with copolymer and pre-exposed with UV light. After coating with PMMA 950 and exposure with an electron beam, an undercut is formed. During evaporation, the angle of the sample can be adjusted. Oxygen is introduced into the chamber after the first layer of metal of about 30 nm is deposited, creating a thin layer of oxide serving as the tunnel barrier. The sample is then tilted and another layer of Al is deposited. The SET is positioned in the vicinity of a QD. The central island of the SET is extended above the QD as shown in Fig. 2.6. The tunnel junctions have a dimension of 50 ± 15 nm $\times$ 50 ± 15 nm.

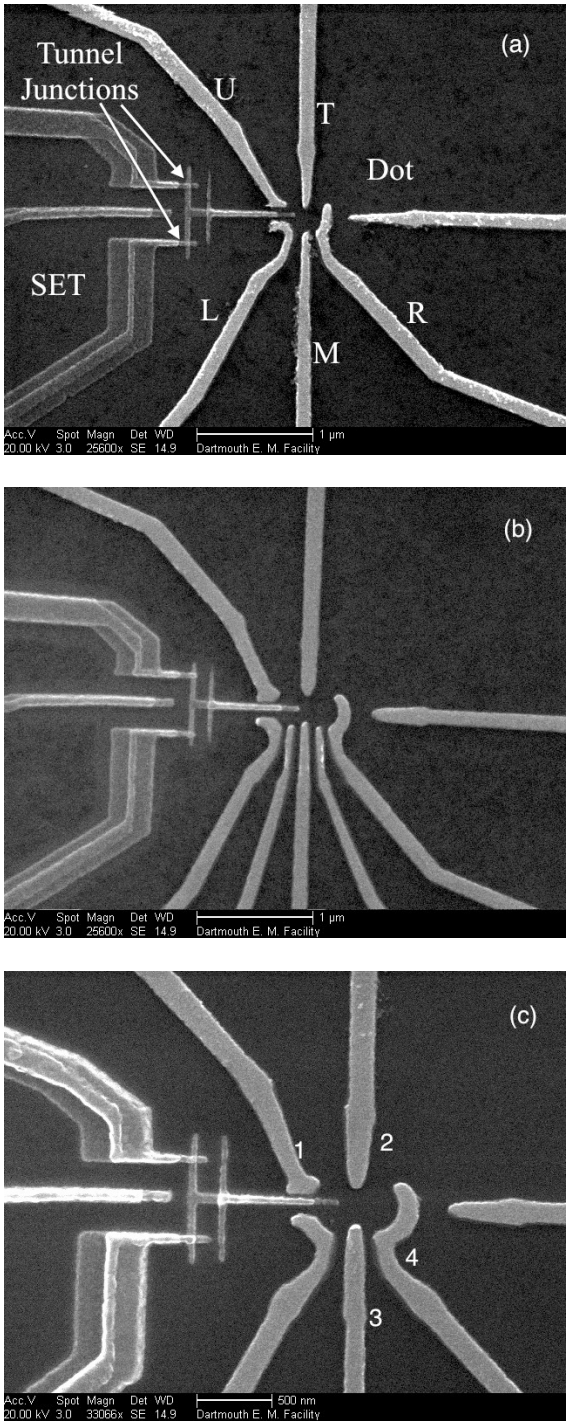

Figure 2.6: Electron scanning micrographs of QD-SET devices with different QD designs

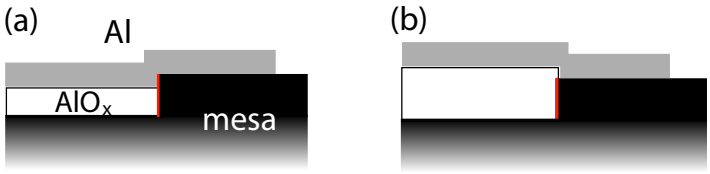

Figure 2.7: Schematics of the mesa edge

The back filling of the mesa etch is critical not only for the Pd dot gates but also for the Al SET. In some samples the surface of the oxide is below the mesa (Fig. 2.7(a)). Subsequently the Al leads to the SET are in contact with the mesa edge. In this case, the SET shows no signs of a high-impedance sub-gap region (Fig. 2.8(a)). We conclude that the high gap currents are a result of the leakage current at the interface of Al and the edge of the mesa (Fig. 2.7(a)). Apparently, the tolerance for leakage of an SET is significantly smaller than that of Pd Schottky gates. To circumvent this problem, we completely seal the edge of the mesa with oxide (Fig. 2.7(b)). In samples fabricated following this procedure, the leakage is further reduced and the superconducting gap of $\sim$1.5 mV is clearly visible in the SET I-V characteristics(Fig. 2.8(b)).

2.3 Cryogenic refrigerators

The ^{3}He Refrigerator (Oxford HelioxAC-V) can cool the sample down to about 0.3 K without using liquid He and is very convenient to operate. The system consists of a pulse tube cryocooler (PTC), an external compressor and a insert with a sorption pump and a ^{3}He pot.

Initially the PTC is switched on to cool its 2nd stage to below 10 K. Meanwhile, the sorption pump is cooled down simultaneously with the 2nd stage. We modify the

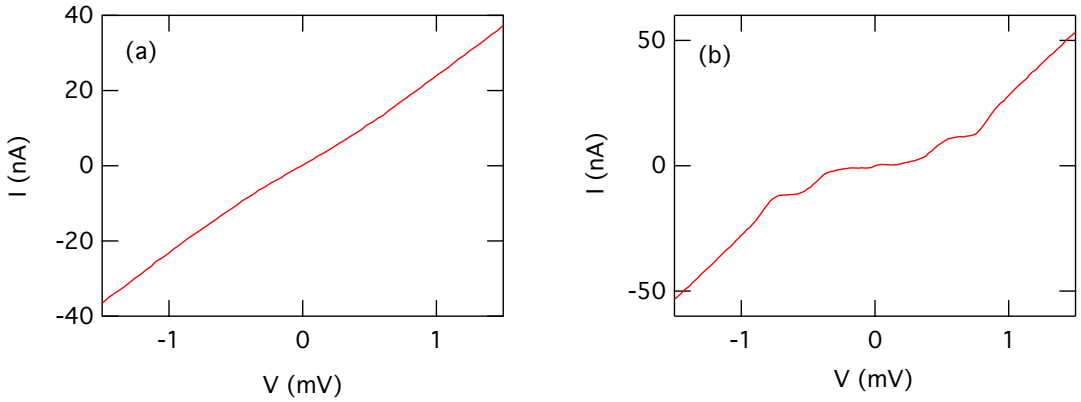

Figure 2.8: SET I-V curves for a mesa (a) not completely sealed; and (b) completely sealed.

standard procedure and keep the heat switch closed at all time during this step to ensure a thermal link between the 2nd stage and the sorption pump. The sorption pump is connected to the ^{3}He dump by keeping Valve 1 (V1) open and starts to pump the ^{3}He gas in the dump as well as any remaining ^{3}He in the pot when it is cooled down to below 20 K. The process is illustrated in Fig. 2.9(a).

When the ^{3}He is completely adsorbed by the sorption pump, V1 is closed to isolate the dump and the sorption pump. The heat switch is turned off to break the thermal link between the 2nd stage and the sorption pump. As the sorption pump warms up with the help of a heater the ^{3}He gas is released into the pot, acting as a thermal link between the 2nd stage and the pot to cool the insert down to about 3 K (Fig. 2.9(b)).

At this point the system is ready for ^{3}He condensation. V1 is opened for a few seconds so that the ^{3}He gas expands into the empty dump, which provides further cooling, allowing liquid to condense and collect at the bottom of the pot. After V1

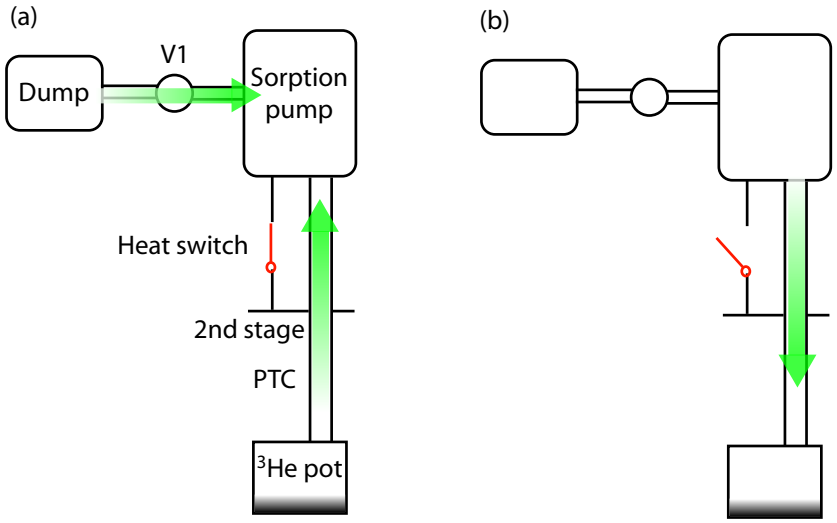

Figure 2.9: Operating principles of ^{3}He refrigerator.

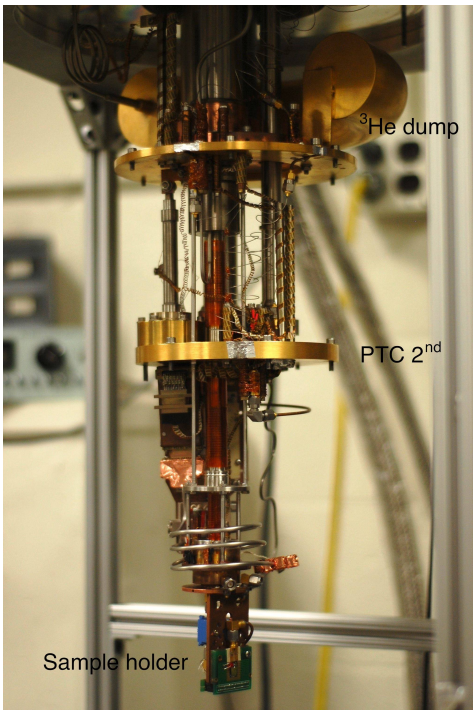

Figure 2.10: The insert of ^{3}He refrigerator.

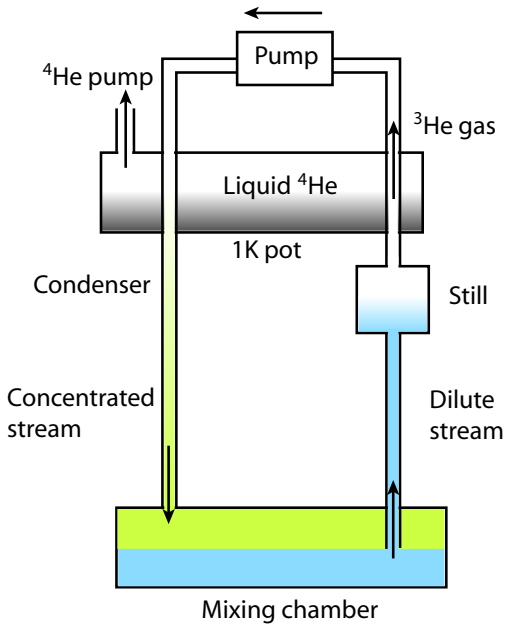

Figure 2.11: Operating principles of a dilution refrigerator.

is closed, the sorption pump heater is turned off and the heat switch is turned on so that the sorption pump can be cooled down to below 10 K by the 2nd stage, pumping the ^{3}He gas from the pot and cooling the insert down to the base temperature of about 0.3 K. The actual cryostat is shown in Fig. 2.10.

To reach temperatures even lower than 0.3 K, a dilution refrigerator will need to be used. Experiments in this thesis have utilized an Oxford Kelvinox Compact as well as an Kelvinox 400, both with a similar principle of operation. Below a critical temperature, the mixture of ^{3}He and ^{4}He separates into two phases: a concentrated phase rich in ^{3}He and a dilute phase rich in ^{4}He. The enthalpy of ^{3}He is different in the two phases, therefore cooling can be obtained by evaporating ^{3}He from the concentrated phase into the dilute phase.

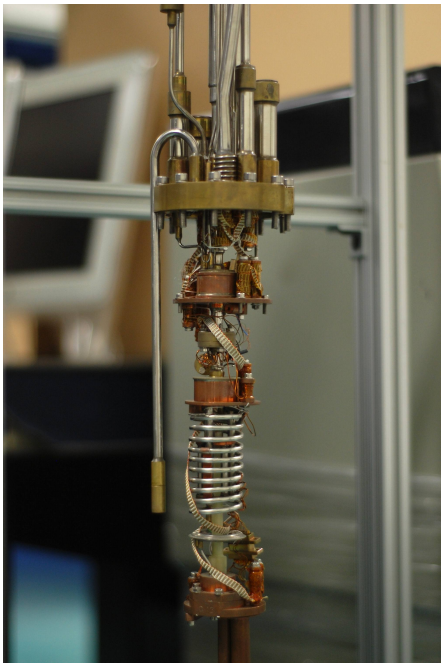

Figure 2.12: The insert of the Kelvinox Compact

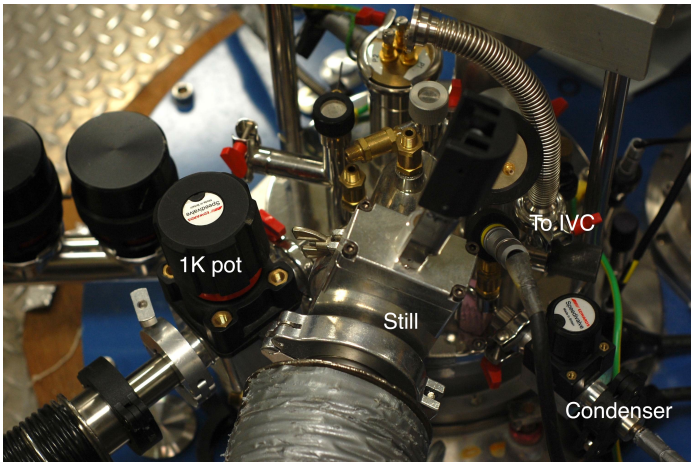

Figure 2.13: The top panel of the Kelvinox 400

2.3 Cryogenic refrigerators

When the dilution refrigerator operates continuously, the system is kept in a dynamic equilibrium, in which the ^{3}He is pumped from the dilute phase in the still and returned into the concentrated phase, as shown in Fig. 2.11. The 1K pot draws liquid ^{4}He from the main bath and is kept at about 1.5 K with constant pumping, allowing the gas mixture to condense into the dilution unit. Kelvinox Compact (Fig. 2.12) has a base temperature of about 60 mK and Kelvinox 400 (Fig. 2.13) can cool down to below 20 mK.

Chapter 3

Si/SiGe single quantum dots: transport measurement

3.1 Single-electron behavior

A QD is a nanostructure in which confinement is imposed, resulting in a quantization of both the energy spectrum and the number of electrons. In a 2DEG the electrons are confined to move in the $x-y$ plane. Additional confinement is imposed by the Pd Schottky gates. Let us first consider a single quantum dot neglecting the quantization of energy levels. Fig. 3.1 is the equivalent circuit of such a system. Following the discussion in Ref. [41], from Kirchhoff's law, the voltages across junctions 1 and 2 are

$$V_1 = \frac{1}{C_\Sigma}\left(V_b(C_g + C_2) - V_g C_g + Q\right) \tag{3.1}$$

$$V_2 = \frac{1}{C_\Sigma}(V_b C_1 + V_g C_g - Q), \tag{3.2}$$

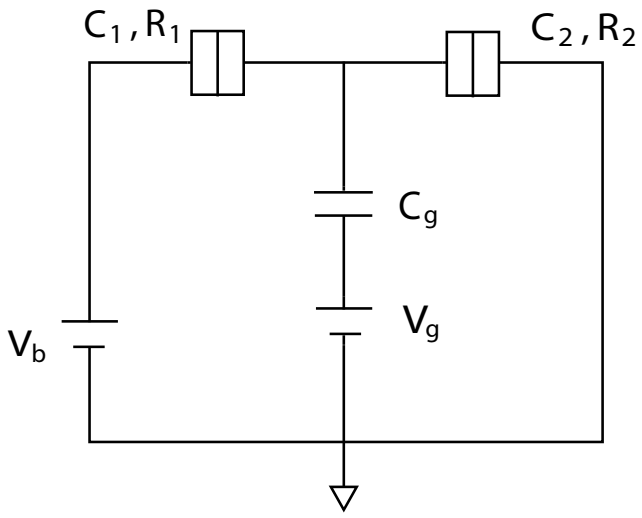

Figure 3.1: Schematic circuit equivalent of a QD

where $C_\Sigma = C_1 + C_2 + C_g$ is the total capacitance and $Q = en$ is the island charge. When tunneling takes place in junction 1, the change in the total energy is

$$\begin{aligned} \Delta U_1^{\pm} &= \frac{Q^2}{2C_\Sigma} - \frac{(Q \mp e)^2}{2C_\Sigma} \mp eV_1 \\ &= \frac{e}{C_\Sigma}\left(-\frac{e}{2} \mp [en + (C_g + C_2)V_b - C_g V_g]\right) \end{aligned} \tag{3.3}$$

Similarly, for junction 2

$$\begin{aligned} \Delta U_2^{\pm} &= \frac{Q^2}{2C_\Sigma} - \frac{(Q \pm e)^2}{2C_\Sigma} \mp eV_2 \\ &= \frac{e}{C_\Sigma}\left(-\frac{e}{2} \mp [en - C_1 V_b - C_g V_g]\right) \end{aligned} \tag{3.4}$$

Eq. 3.3 and 3.4 can be used to generate a stability plot in the $V_b - V_g$ plane. The boundary lines are given by setting $\Delta U_{1,2} = 0$. The shaded area in Fig. 3.2 are called

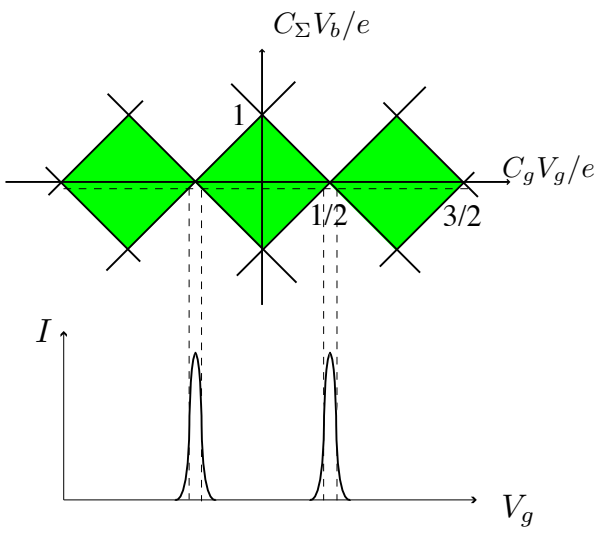

Figure 3.2: A stability diagram with $C_2 = C_g$ and $C_1 = 2C_g$

Coulomb diamonds. Inside each diamond the number of electrons is constant, hence Coulomb blockade is established. If we keep the source-drain bias V_b a small constant and scan V_g, we will observe periodic conduction peaks with period $\Delta V_g = \frac{e}{C_g}$, which are the Coulomb oscillations.

3.2 Device and measurement set-up

The Pd Schottky gates are energized to form a QD. When negative voltage is applied, the gates deplete the underlying 2DEG so that single electron phenomena can be observed. Tunnel barriers that are tuned by the gate voltages can isolate the 2DEG and form a well-defined QD. To observe Coulomb oscillations, one usually sweeps the voltage applied on one of the dot gates while keeping all the other gates at a constant voltage. For instance we can apply constant voltage on gates U, L, M, R in Fig. 2.6(a)

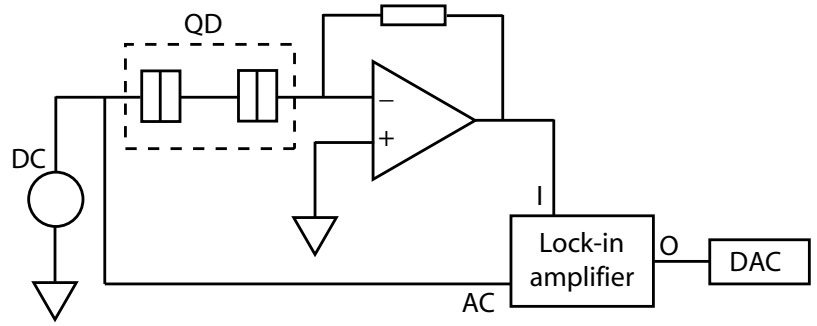

Figure 3.3: Schematic diagram of QD transport measurement.

and scan gate T.

Fig. 3.3 is a schematic diagram of the typical measurement circuit. The ohmic contacts provide connections to the source and drain of the QD. A dc voltage V is combined with a small ac signal v generated by the lock-in amplifier (Signal Recovery 7225) and applied at the source of the QD. The root mean square (rms) of v is chosen between 3 and 30 μV. The drain is connected to a lab-built current amplifier providing a path to ground for the current. The current is usually amplified by 10^7 to 10^9 times before returned to the lock-in, which then demodulates the signal and produces a dc output of the QD current I caused by the small voltage signal. By dividing I by v the differential conductance G_d can be obtained.

There are various ways to combine two voltage sources. The first is to use a summing amplifier which provides reliable results for a wide range of signals but requires battery for operation. Another option is to use a passive adder of dc and ac voltages. The circuit shown in Fig. 3.4, from Ref. [42], produces an output of $V \times 10^{-3} + v \times 10^{-5}$. We can also use a lab-built voltage reference by floating it internally and connecting its 'ground' to an external voltage source. The output

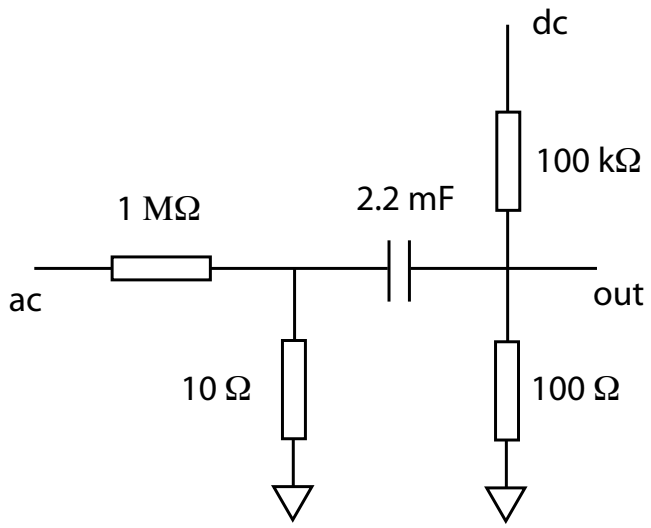

Figure 3.4: Circuit diagram for combining dc and ac bias voltages

will be a combination of the reference signal and the signal generated by the voltage reference itself. This is especially useful if a constant dc offset much larger than the external small voltage signal is required since one can apply a voltage divider on the external voltage source to achieve a more stable voltage output.

3.3 Coulomb blockade measurement

The top gate structure enables versatile control over the tunnel barriers and island potential of the QD. Fig. 3.5 shows an example of measured Coulomb oscillations, displaying the change of conductance as a function of the voltage applied on the gate. A conductance peak corresponds to the addition of one electron. The period of oscillations ΔV_g can be used to compute the coupling capacitance C_g of the gate to the QD. For instance in Fig. 3.5 $\Delta V_g \approx 8$ mV and $C_g \approx 20$ aF.

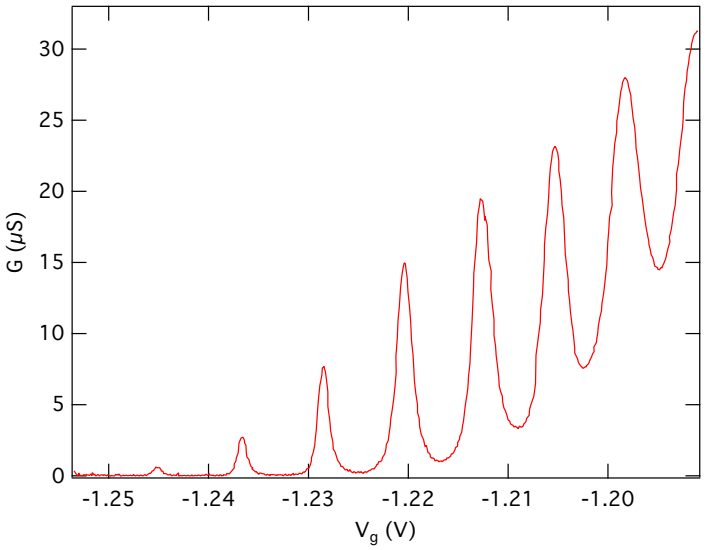

Figure 3.5: Coulomb oscillations of a Si/SiGe QD

When both V_g and the bias voltage V_{SD} are varied, a stability plot of Coulomb diamonds can be obtained. One such example is shown in Fig. 3.6, where the transition between an open QD to a relatively closed QD can be seen as V_g becomes more negative. The span ΔV_{SD} of the diamond in V_{SD} reveals the total capacitance C_Σ of the QD and subsequently the charging energy E_c. For the lowest diamond in Fig. 3.6 (between $V_g = -0.84$ and -0.81 V) $C_\Sigma \approx 46$ aF and $E_c = e^2/C_\Sigma \approx 1.7$ meV. It can be seen in Fig. 3.6 that as the QD becomes more pinched-off the diamonds become bigger and correspondingly E_c increases. This is an indication that the QD has reached the few-electron regime since the capacitances become smaller as the QD becomes smaller and more isolated.

Both Fig. 3.5 and 3.6 are measured at 0.3 K. The stable behavior of the QD demonstrated by Fig. 3.6 also suggests that the low-leakage fabrication process is functioning well. In Fig. 3.6 we observe features of the Kondo effect, whose signature is

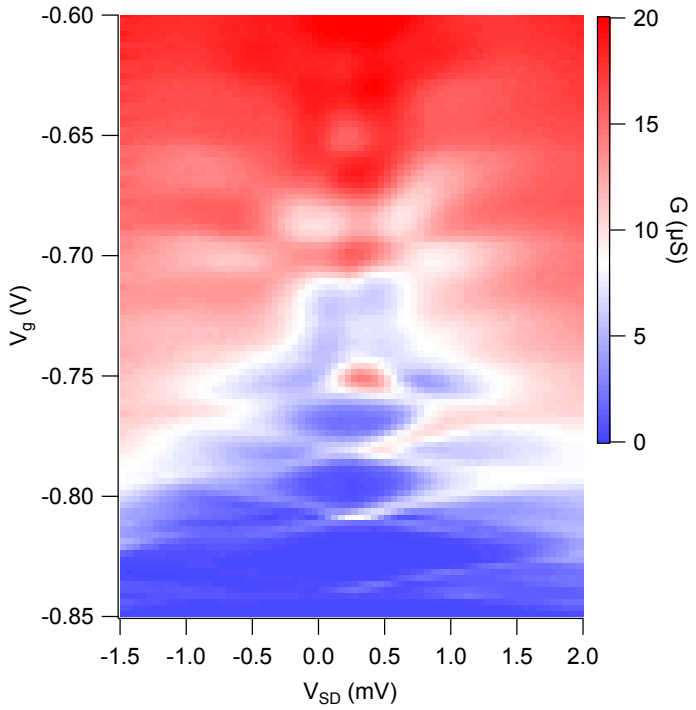

Figure 3.6: Differential conductance in a QD vs bias and gate voltages showing multiple Coulomb diamonds

the enhancement of conductance inside the Coulomb diamond, which will be discussed in detail in the following chapter.

Chapter 4

Valley Kondo effect

4.1 Theoretical background

4.1.1 Pure spin Kondo effect

From Chapter 3 it is clear that charge quantization in a QD is a result of potential confinement and weak tunnel coupling to the leads. If the tunnel coupling is increased by reducing the tunnel barriers but the number of charges still remains discrete, localized electrons in the QD have a chance to interact with delocalized electrons in the leads and virtual processes involving higher order tunneling have to be taken into account. When spin plays a role, these virtual processes give rise to the Kondo effect in QDs, resembling the interaction between magnetic impurities and conduction electrons in metals, from which the name originates.

The spin 1/2 Kondo effect comprehensively studied in GaAs QDs [43, 44] is usually observed when there is an odd number of electrons in the QD, in which the spin of

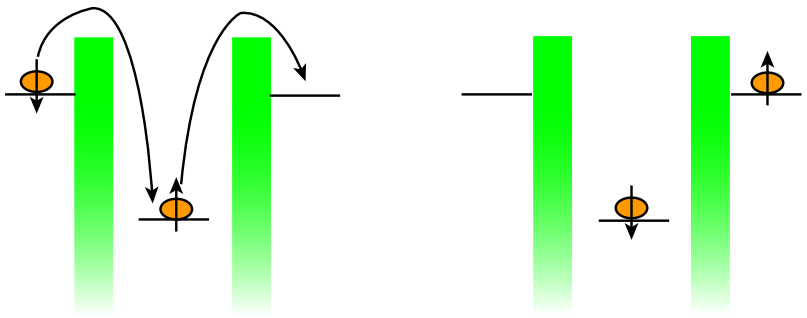

Figure 4.1: Schematic diagram of a spin 1/2 Kondo process

an unpaired electron is screened by spins in the leads to form a singlet, resulting in a conductance resonance at zero dc bias. An example is illustrated in Fig. 4.1, in which a spin-up electron tunnels off the QD and a spin-up electron from the lead tunnels on the QD. When spin degeneracy is lifted by a magnetic field B, the spin-Kondo resonance splits into two peaks at $eV_{\mathrm{SD}} = \pm g\mu_{\mathrm{B}}B$, g being the Landé factor and μ_{B} the Bohr magneton [45].

The Anderson Hamiltonian [46] is applied in Ref. [45] to establish a model for the Kondo effect in QDs:

$$H = \sum_{ik\sigma} \epsilon_{k\sigma} c^{\dagger}_{ik\sigma} c_{ik\sigma} + \sum_{\sigma} \epsilon_{\sigma} a^{\dagger}_{\sigma} a_{\sigma} + U n_{\uparrow} n_{\downarrow} + \sum_{ik\sigma} (V_{ik\sigma} c^{\dagger}_{k\sigma} a_{\sigma} + \mathrm{H.c.}), \tag{4.1}$$

where $c^{\dagger}_{k\sigma}$ ($c_{k\sigma}$) creates (destroys) an electron with energy $\epsilon_{k\sigma}$, momentum k and spin σ in lead $i \in L, R$ and $a^{\dagger}_{\sigma}$ (a_{σ}) are the creation and annihilation operators for a spin-σ ($\sigma \in \uparrow, \downarrow$) electron on the QD. The third term is the Coulomb interaction taken to forbid double occupancy and the fourth term describes the transfer of electrons between the leads and the QD.

The current through the QD can be expressed as

$$J = \frac{e}{\hbar}\sum_{\sigma}\int d\omega[f_L(\omega) - f_R(\omega)]\Gamma_\sigma(\omega)\left[-\frac{1}{\pi}\mathrm{Im}G^r_\sigma(\omega)\right], \tag{4.2}$$

where $f_{L,R}$ are the Fermi functions in the leads and $(-1/\pi)\mathrm{Im}G^r_\sigma(\omega)$ is the density of states, G^r_σ being the Fourier transform of the retarded Green function. Tunnel couplings to the leads are defined as $\Gamma^i_\sigma(\omega) = 2\pi\sum_{ik}|V_{k\sigma}|^2 \times \delta(\omega - \epsilon_{k\sigma})$ and $1/\Gamma_\sigma(\omega) = 1/\Gamma^L_\sigma(\omega) + 1/\Gamma^R_\sigma(\omega)$ in Eq. 4.2. Calculations in Ref. [45] find logarithmic divergences signaling Kondo peaks at $\mu_{L(R)} \pm \Delta\epsilon$ in the density of states, where $\mu_{L(R)}$ is the chemical potential of the left (right) lead and $\pm\frac{1}{2}\Delta\epsilon$ is the Zeeman splitting. Therefore, the distance between the two Kondo peaks in a magnetic field is **twice** the Zeeman splitting.

More recently the observation of Kondo effect has been expanded to QDs with integer spin [47, 48, 49, 50, 51], in which singlet-triplet transition is usually involved and the interference of two available channels can lead to the two-stage Kondo effect [52, 53, 54].

4.1.2 Kondo effect in Si with valley degree of freedom

The valley degree of freedom of conduction band electrons is one of several intriguing properties distinguishing Si from III-V materials. The six-fold valley degeneracy in bulk Si is reduced to two-fold in Si/SiGe heterostructures due to the confinement of electrons in the 2DEG. The resulting valley splitting Δ in strained Si quantum wells has been studied using conventional transport [55, 56] and is typically of order 0.1 meV. The addition of the valley degree of freedom allows for a new set of Kondo phenomena to emerge, since both spin and valley indices can be screened. Kondo

effects in Si/SiGe QDs have rarely been reported [57], although there have been recent studies of dopants in a Si fin-type field effect transistor [58, 59]. This is perhaps not surprising, since for the valley Kondo effect to occur, the energy associated with the Kondo temperature T_{K} must be larger than the valley splitting Δ, i.e. $k_{\mathrm{B}}T_{\mathrm{K}} > \Delta$ where k_{B} is the Boltzmann constant, a rather stringent condition. Nonetheless, how the valley degeneracy in Si affects the Kondo effect in Si/SiGe QDs has been investigated theoretically [60, 61] and found to share some resemblance with carbon nanotubes [62]. The following introduction is based on Ref. [60, 61].

The Hamiltonian expressed in Eq.4.1 is expanded to

$$\begin{aligned} H = &\sum_{ikm\sigma} \epsilon_{km\sigma} c^{\dagger}_{ikm\sigma} c_{ikm\sigma} + \sum_{m\sigma} \epsilon_{m\sigma} a^{\dagger}_{m\sigma} a_{m\sigma} + U \sum_{m'\sigma' \neq m\sigma} n_{m'\sigma'} n_{m\sigma} \\ &+ \sum_{ikm\bar{m}\sigma} (V_{ikm\bar{m}\sigma} c^{\dagger}_{ikm\sigma} a_{\bar{m}\sigma} + \mathrm{H.c.}), \end{aligned} \tag{4.3}$$

where $c^{\dagger}_{ikm\sigma}$ ($c_{ikm\sigma}$) creates (destroys) an electron with momentum k, valley index $m \in o, e$, spin $\sigma \in \uparrow, \downarrow$ and energy $\epsilon_{km\sigma}$ in lead $i \in L, R$ and $a^{\dagger}_{m\sigma}$ ($a_{m\sigma}$) are the creation and annihilation operators for an electron with valley m and spin σ on the QD. The third term is the Coulomb interaction taken to forbid double occupancy and the remaining term describes the transfer of electrons between the leads with valley index m and the QD with valley index $\bar{m}$.

When $V_{ik(m=\bar{m})\sigma} < V_{ik(m\neq\bar{m})\sigma}$, the valley mixing is relatively strong. The ground state of H is a combination of terms that can be visualized graphically as processes that involve the hopping of an electron from the left lead to the right lead. Each distinct process can give rise to a peak in the conductance if the amplitude of the process is large enough while unobserved processes indicate a small tunneling matrix

element. The position of the peak can be read off from the energy change of the electron in the process, while the height of the peak depends on the tunneling amplitude that produces it.

4.2 Measurement in perpendicular magnetic field

We measure the differential conductance of a Si/SiGe QD (Sample I) with lock-in techniques, using an ac bias of 3 μV. The sample is cooled down to about 60 mK, corresponding to an electron temperature of $T_e \approx 150$ mK and oriented perpendicular to the magnetic field.

Interesting conductance enhancements appear in the Coulomb blockade region, as shown in the stability diagram of the QD differential conductance G in Fig. 4.2. The x-axis is the dc bias voltage V_{SD} (a slight offset is present) while the gate voltage V_g is displayed on the y-axis. There is a lower Coulomb diamond between $V_g \approx -0.85$ and -0.69 V and an upper one starting at $V_g \approx -0.69$ and extending towards the top of the figure. The relatively large size of this lower diamond (V_{SD} between ± 3 mV) suggests that the QD is in the few-electron regime. It also shows co-tunneling features consisting of two roughly vertical regions of enhanced conductance for $V_{\mathrm{SD}} < -0.5$ mV and $V_{\mathrm{SD}} > 0.9$ mV that depend only weakly on V_g. The inelastic co-tunneling is due to virtual transitions to an excited state with excitation energy of about 0.8 meV, indicating that it involves a change in orbital state rather than valley state, for which the excited state energies are typically < 0.2 meV. The co-tunneling feature has important implications for electron number N in the QD [63]. Each energy level can be doubly occupied. For N odd, the inelastic co-tunneling can always happen via the energetically favorable singly-occupied level instead of a higher level. Therefore,

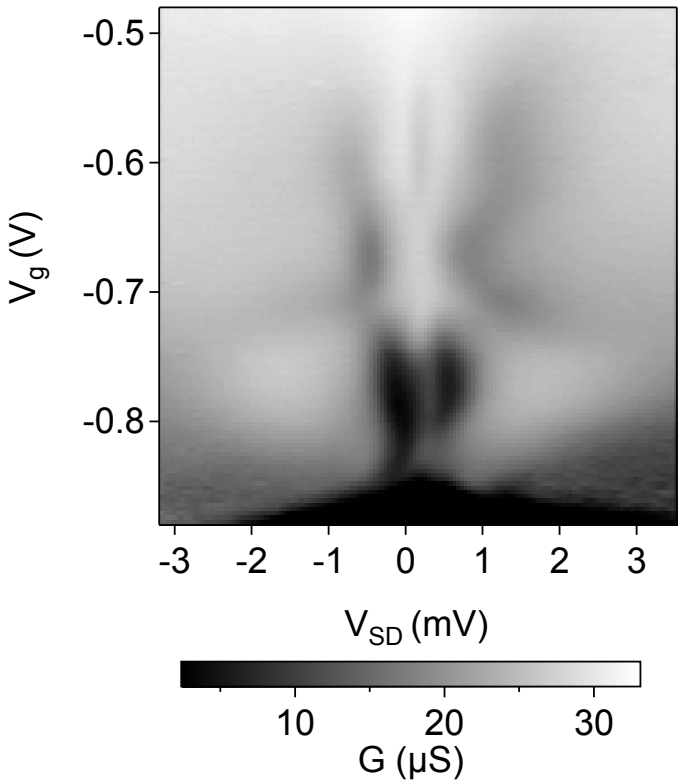

Figure 4.2: Stability diagram of differential conductance showing Kondo effect

there will not be an abrupt enhancement of conductance at a certain bias voltage in the Coulomb blockade. For N even on the other hand, for a co-tunneling event to take place it has to borrow a higher level and can only happen when the bias voltage reaches the threshold determined by the energy level spacing, yielding a sudden step in the conductance. Thus the presence of the co-tunneling in the lower diamond identifies it as corresponding to an even-electron-number state. The upper diamond must therefore correspond to an odd-electron-number state. We refer to the upper (lower) diamond as the odd(even)-number diamond. The Kondo effect in Si/SiGe QDs is forbidden for $N = 4m, m = 0, 1, 2, ...$ [61] since the spin and valley states for a particular orbital state are filled. Therefore, the even-number diamond corresponds to $N = 4m + 2$ while the odd-number diamond corresponds to $N = 4m + 3$.

The temperature dependence of the resonances in the odd- and even-number diamonds is shown in Fig. 4.3(a) and (b), respectively, while their magnetic field dependence is shown in Fig. 4.3(c) and (d). As can be seen in Fig. 4.3(a) and (b), the resonances weaken as the temperature increases and vanish for $T > 1.8$ K, verifying the presence of Kondo physics. There are several notable aspects of these resonances that contradict the spin 1/2 Kondo picture, such as a split resonance that coalesces into a single peak in the odd-number diamond and a single resonance in the even-number diamond that does not shift in V_{SD} as B is increased. These seemingly counterintuitive phenomena are indicators of valley Kondo physics in our QD.

Focusing on the field dependence of these features in Fig. 4.3(c), as B is increased the two peaks broaden and coalesce, becoming indistinguishable at B=1 T. The processes resulting in the Kondo effect for a QD with $N = 4m + 3$ are illustrated in Fig. 4.4(a). Theory predicts three peaks in the absence of B when the valley index is

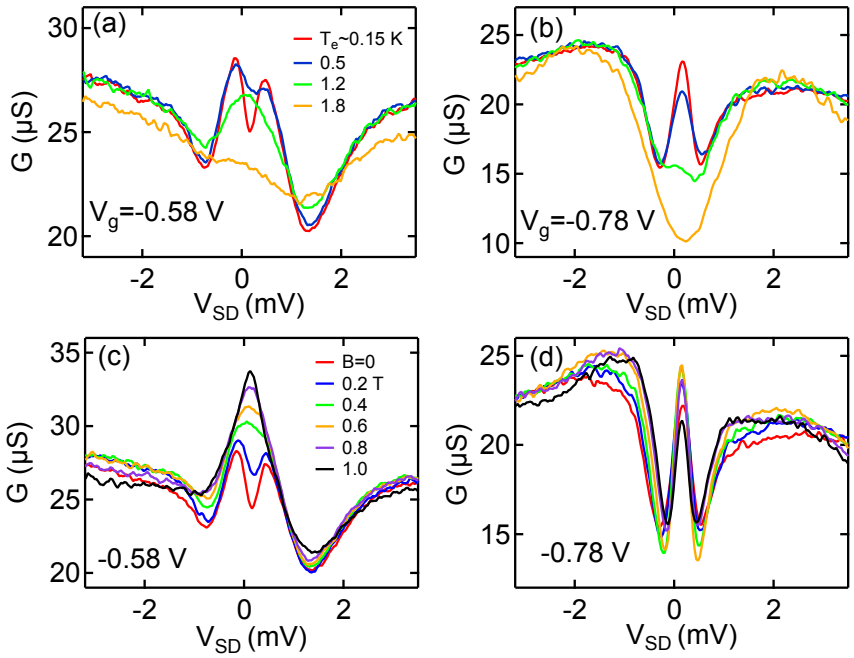

Figure 4.3: Temperature and field dependence of the Kondo resonances at $V_g = -0.58, -0.78$ V

conserved: a peak at zero bias that involves a spin flip, commonly observed in GaAs QDs; and two valley side peaks that are due to changes in both spin and valley indices as the electrons tunnel through the QD [60]. A magnetic field should split each valley Kondo peak into three peaks, the distance between neighboring peaks being $g\mu_{\mathrm{B}}B$. In Fig. 4.4 two valley states with energy difference Δ are labeled by o and e. Note, however, that since parity is not a good quantum number in the device, the states are not necessarily odd and even in the z-coordinate.

In the upper panel ($B = 0$), the orange arrows correspond to the conventional spin 1/2 Kondo effect that results in a central peak; note that the processes involve tunneling to and from an e valley state. In contrast, the solid blue arrows illustrate a process in which an electron occupying the o valley state tunnels off the QD, and another electron from the lead tunnels on to the QD to occupy the e state, resulting in the side peaks. A spin-reversed process is illustrated by the dashed lines. The absence of the central peak in our experimental results suggests that the tunneling involving an odd valley is stronger than the pure even-valley tunneling ($V_{ikm(\bar{m}=e)\sigma} < V_{ikm(\bar{m}=o)\sigma}$) and the Kondo temperature corresponding to the inter-valley process is higher than the spin-1/2 process. Therefore, at finite temperature, the side peaks are easier to observe while the center peak is obscured.

In this picture, the separation in V_{SD} of the two side peaks is twice the zero-field valley splitting Δ in the QD, so $\Delta \approx 0.28$ meV. A magnetic field lifts the spin-degeneracy of each valley state. In the lower panel ($B > 0$), each valley state splits into two spin states. A spin-down (up) electron in the o state tunnels off the QD while a spin-up (down) electron tunnels on to the e state, as indicated by the solid (dashed) arrows, swapping both valley and spin indices. The other two processes

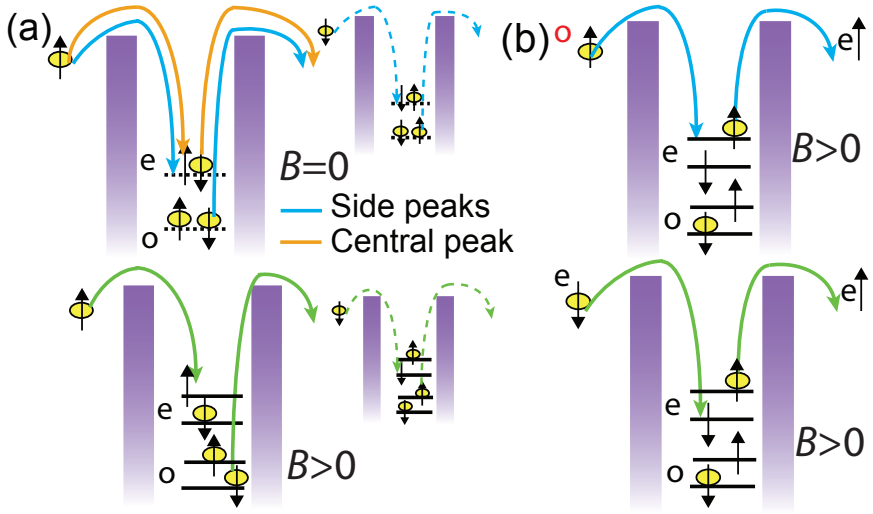

Figure 4.4: Single-particle processes that can be associated with each conductance peak. The many-body wavefunction is a complicated combination of terms each of which is also associated with a process.

remain degenerate, swapping only the valley index while preserving the spin index. As a result, the four processes generate three resonances in finite B field. The resulting splitting broadens the two Kondo peaks and they coalesce into one peak, as shown in Fig. 4.3(c).

In the even-number diamond, there is a single resonance at zero bias. As shown in Fig. 4.3(b) the height of the resonance decreases monotonically with temperature, vanishing at ∼1.8 K, indicating a Kondo temperature of T_K ∼3-4 K.

Surprisingly, as B is increased this central resonance does not split, as shown in Fig. 4.3(d). In Fig. 4.5 where $V_g = -0.83$ V the FWHM of the Kondo resonance is about 0.25 meV, comparable to the Zeeman splitting at $B = 1$ T and the Zeeman-

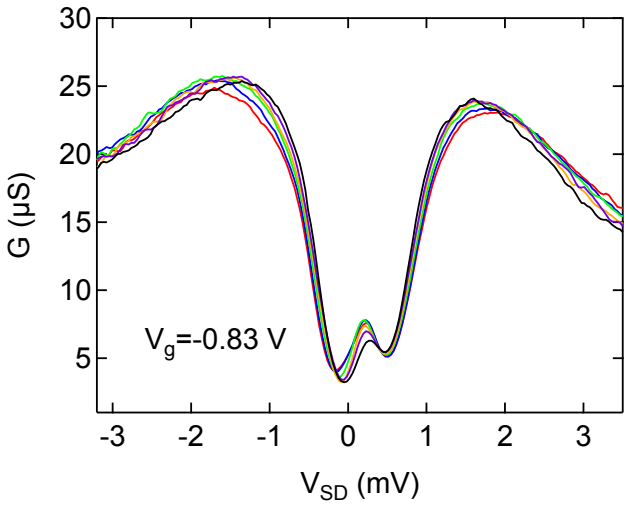

Figure 4.5: Field dependence of the Kondo resonances at $V_g = -0.83$ V. The color legend is the same as in Fig. 4.3.

split peaks would be resolved. However we still only observe a single peak. In fact, a peak at zero dc bias that persists in a non-zero magnetic field is expected to be a signature of pure valley Kondo effect, associating with a process in which the valley index is not conserved [60, 61]. For $B_\perp \neq 0$ the center peak involving only valley screening (upper panel of Fig. 4.4(b)) dominates while the side peaks (lower panel of Fig. 4.4(b)) are suppressed. This indicates that the Kondo temperature relating to the pure valley process is higher than that of the spin process, a result of strong valley mixing $V_{ik(m=\bar{m})\sigma} < V_{ik(m\neq\bar{m})\sigma}$. Also, with the magnetic field perpendicular to the 2DEG, we expect some dependence of the tunneling matrix elements on $B_\perp$, which might also be the reason why the peak height as well as the co-tunneling features show non-monotonic dependence on $B_\perp$.

4.3 Measurement in parallel magnetic field

The same sample is also measured in a parallel magnetic field B inside Kelvinox 400 with a base temperature of 20 mK and once again we observe non-splitting Kondo peaks. Fig. 4.6 shows the stability plot of two charge states when the magnetic field is off. A Kondo resonance at zero dc bias emerges in both charge states. When B is turned on, the center peak in both diamonds persists without splitting even at $B \geq 3$ T, as demonstrated in Fig. 4.7. Since the g factor in Si is about 5 times bigger than that in GaAs, 3 T here is comparable to 15 T for a GaAs based QD.

As can be seen in Fig. 4.7, the maximum of the resonances is gradually suppressed by the increasing B. In Fig. 4.8 we plot the height for $V_g = -0.75$ V as a function of B. The red line in the high field regime is a fit showing logorithmic dependence on the magnetic field. It is clear that although B is unable to split the Kondo peak, the energy associated with the magnetic field diminishes the Kondo effect.

In addition, we measure a different QD (Sample II). Again we find enhancement of conductance in two consecutive Coulomb diamonds. In one diamond the resonance behaves in a similar fashion as Sample I, which decreases with increasing B field without splitting. As shown in Fig. 4.9, at $B = 0$ there is a single Kondo resonance. It is gradually reduced as B is increased and at $B = 2.5$ T the Coulomb blockade is fully recovered.

In a second diamond some side peak features are resolved. In Fig. 4.10 the curves are offset by 60 nS/T$\times|B|$. The center peak decreases with rising B without splitting. There are traces of two side peaks, indicated by the dashed lines, which move towards the center. After converging at about 3.5 T they move away from each other

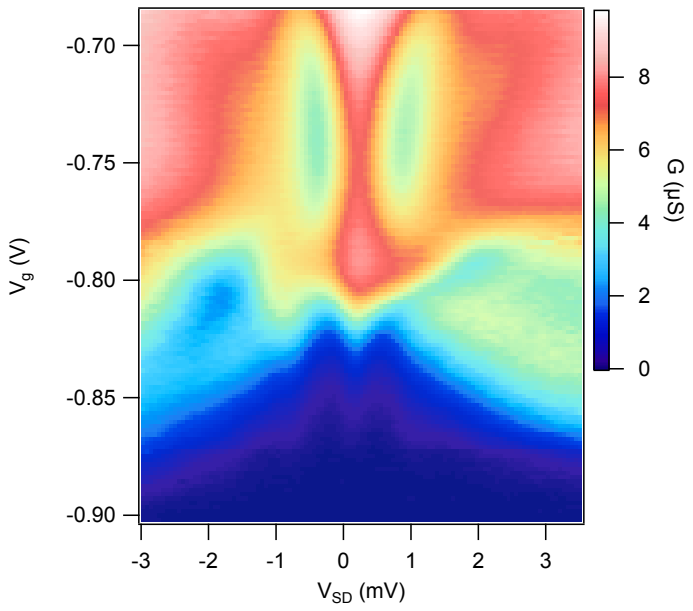

Figure 4.6: Stability diagram showing Kondo effect in two charge states

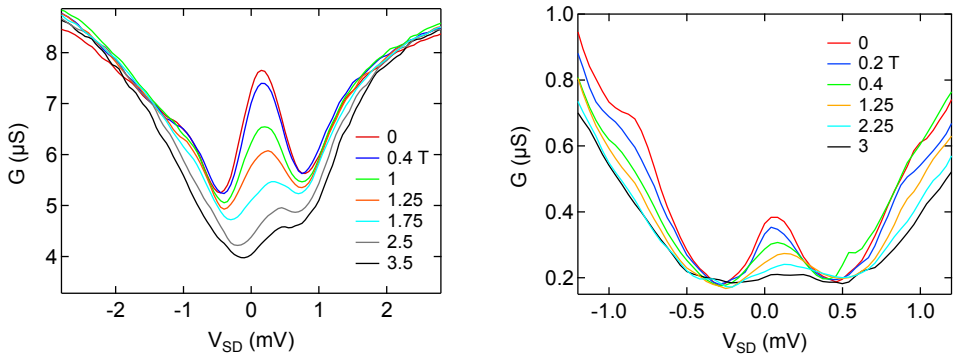

Figure 4.7: B dependence of the Kondo resonance for $V_g = -0.75$ V (left) and $V_g = -0.83$ V (right)

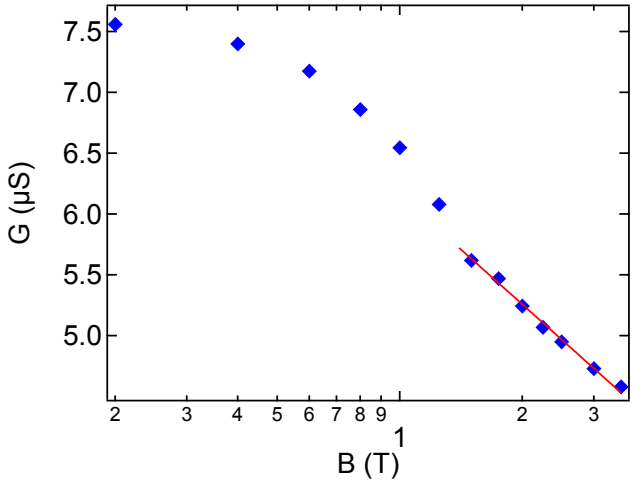

Figure 4.8: Magnetic field dependence of the peak height at $V_g = -0.75$ V. Data are plot as blue markers and the red line is a logorithmic fit.

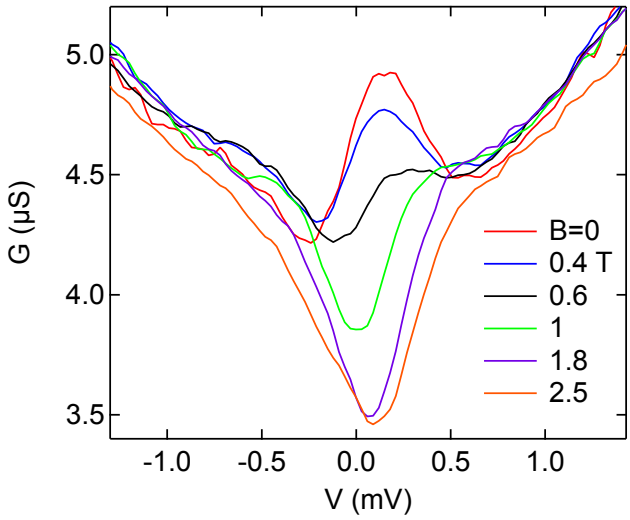

Figure 4.9: Magnetic field dependence of the Kondo resonance in the first Coulomb diamond of Sample II

again. These features are very likely due to the Zeeman splitting of the valley side peaks similar to that illustrated in Fig. 4.4(a), revealing a zero-field valley splitting of about 0.35 mV. The g factor extracted from the two dashed lines are about 1.8 and 1.5 respectively, smaller than but comparable to the standard value of $g = 2$. The asymmetry inside the Coulomb blockade suppresses the Kondo peak at the positive bias, resulting in very weak signal that is hard to read. Nonetheless, the data demonstrate interplay between the spin and valley degrees of freedom.

4.4 Discussion

The center peak that we repeatedly observe is rather unusual. First, it suggests that valley index is not always conserved during tunneling, a subject of some debate [62, 60, 59, 64, 65]. There is a fair chance that hopping between different valley states is allowed due to the miscut in the Si/SiGe heterostructure. Secondly, for the perpendicular field data, given a non-zero Δ, the QD electrons must occupy an excited state rather than the ground state viewed in terms of single-particle levels (see Fig. 4.4(b)). This is allowed energetically since by forming the many-body state with the leads, the system gains energy on the order of $k_{\mathrm{B}}T_{\mathrm{K}} \approx 0.4$ meV, estimated from the FWHM of the central peak, in good agreement with the temperature at which the resonance disappears. Assuming $\Delta \approx 0.28$ meV in this even-number diamond, similar to that in the odd-number diamond, we have $\Delta < k_{\mathrm{B}}T_{\mathrm{K}}$, recovering the condition for the valley Kondo effect to be observed.

The experiments demonstrate that the Kondo effect in Si/SiGe QDs can be very different due to the valley degree of freedom.

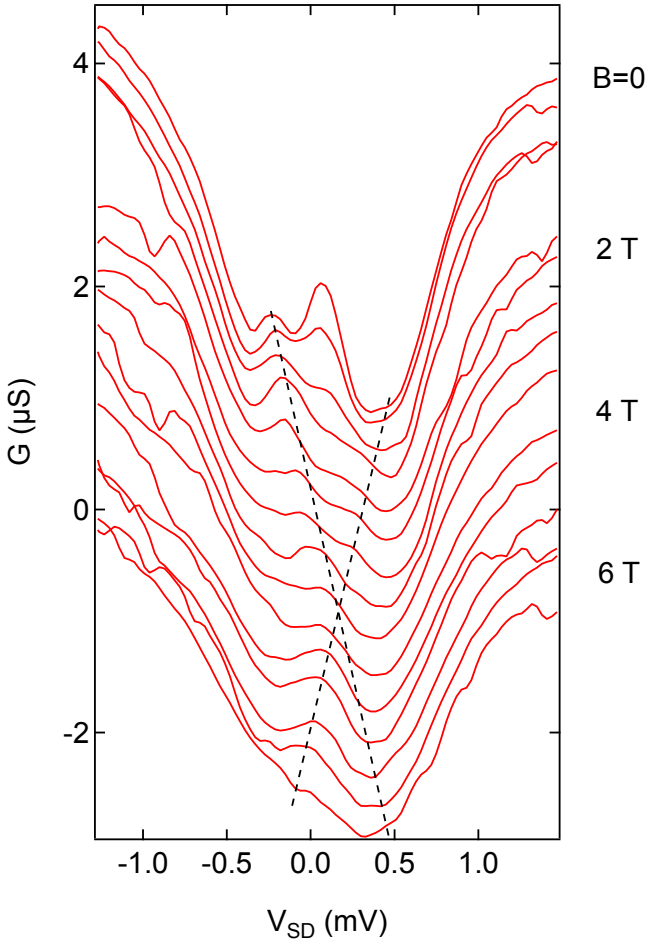

Figure 4.10: Magnetic field dependence of the Kondo resonances in the second Coulomb diamond of Sample II. The center peak is reduced by the magnetic and the side peaks reveal information about both the valley and Zeeman splittings.

Chapter 5

Superconducting single-electron transistor

5.1 Introduction

The SET, first reported by Fulton and Dolan[66], is a sandwich structure of $Al/Al_2O_3/Al$ as shown in Fig. 2.6. In the normal state, an SET is essentially a QD with a small energy level separation, and the discussion on QDs in Chapter 3 applies. Al has a critical field of 0.01 T and a critical temperature of 1.2 K, below which it becomes superconducting. For a superconducting SET, the carriers are Cooper pairs and quasiparticles, as opposed to electrons in the normal state.

An SET consists of two superconductor-insulator-superconductor (SIS) Josephson junctions. For a single SIS junction, the energy required to break a Cooper pair into two quasiparticles is the superconducting gap $2\Delta_i$. When the bias voltage is larger

than $2\Delta_i$, quasiparticles are the main carriers, and the tunneling is dissipative. At zero bias, a current can also occur as a result of coherent Cooper pair tunneling. In order to observe well-defined Coulomb blockade effects, the Coulomb energy must be much larger than the thermal energy, i.e. $e^2/C_\Sigma \gg k_B T$. Additionally , the quantum fluctuations in the particle number must be sufficiently small that each oscillation peak can be well resolved. Starting from the Heisenberg uncertainty relation[41]:

$$\Delta E \Delta t > h \tag{5.1}$$

where $\Delta E \sim e^2/C_\Sigma$, $\Delta t \approx RC_\Sigma$, R being the tunnel resistance,

$$R \gg \frac{h}{e^2} = 25.8 \text{ k}\Omega \tag{5.2}$$

For two junctions in series, the energy requirement for quasiparticle current becomes :

$$eV_{bias} > 4\Delta_i \tag{5.3}$$

Inside the subgap regime where $eV_{bias} < 4\Delta_i$, current peaks arise mainly due to the Josephson-quasiparticle (JQP) cycle and the double Josephson-quasiparticle (DJQP) cycle [67], illustrated in Fig. 5.1. For a JQP process, a Cooper pair tunnels into the island, increasing the charge number by two, followed by two subsequent tunneling of quasiparticles out of the island and the charge number returns to the original value (Fig. 5.1(a)). For a DJQP process, a Cooper pair tunnels into the island. After a quasiparticle tunnels out, the remaining quasiparticle forms a Cooper pair with another electron, leaving a hole in the island. The newly formed Cooper pair tunnels out and an electron tunnels into the island to fill the hole (Fig. 5.1(b)). If the SET

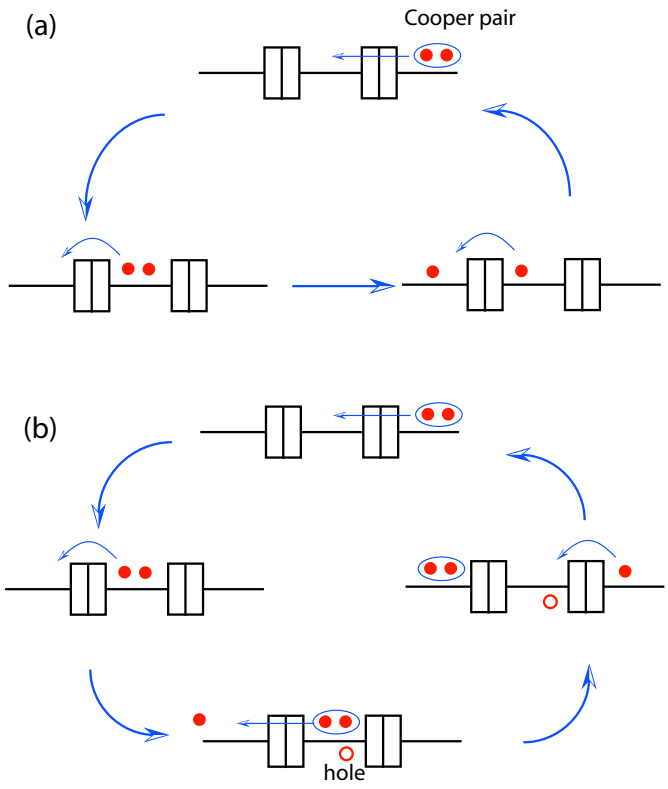

Figure 5.1: Illustrations of (a) JQP and (b) DJQP tunnelings

is biased near a JQP or DJQP resonance, a small change of the gate voltage, or the island potential, will result in rapid variation of the conductance. This property of the SET can be exploited to perform charge sensing.

5.2 Results of dc measurement

5.2.1 Characteristics of superconducting SET

For a dc-only measurement a circuit similar to that illustrated in Fig. 3.3 can be used, replacing the QD with the SET. However for a combined dc and rf measurement the

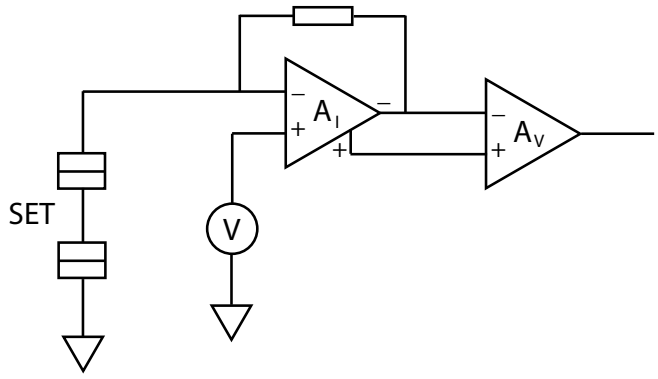

Figure 5.2: Measurement circuit for an internally grounded SET

SET will have to be internally grounded as shown in Fig. 5.2. Since the voltage of $-$ and $+$ inputs of the current amplifier A_I are maintained the same, the source and drain voltage can be applied via the $+$ port. The voltage amplifier A_V reads the difference between the $+$ and $-$ outputs, obtaining the SET current.

Here we demonstrate the measurement of a superconducting SET with the design shown in Fig. 2.6(a). Fig. 2.8(b) is the I-V curve of the SET. The superconducting gap is about 1 mV, with features of JQP/DJQP cycles at the shoulder, and supercurrent at zero bias. The SET is responsive to both its own gate and the nearby dot gates. Fig. 5.3 shows the Coulomb oscillations when the SET is biased at -0.35 mV and the voltage on gate U (see Fig. 2.6(a)) is varied.

To have a more visual understanding of the SET behavior, we can do a 2-dimensional sweep with the lock-in and generate a stability diagram as shown in Fig. 5.4. The voltage on the SET gate is varied between -0.2 to 0.2 V, and the source-drain bias is swept between -1.2 to 1.2 mV. Clear oscillations of differential conductance can be seen. Peaks arising from Cooper pair (CP), DJQP and JQP tun-

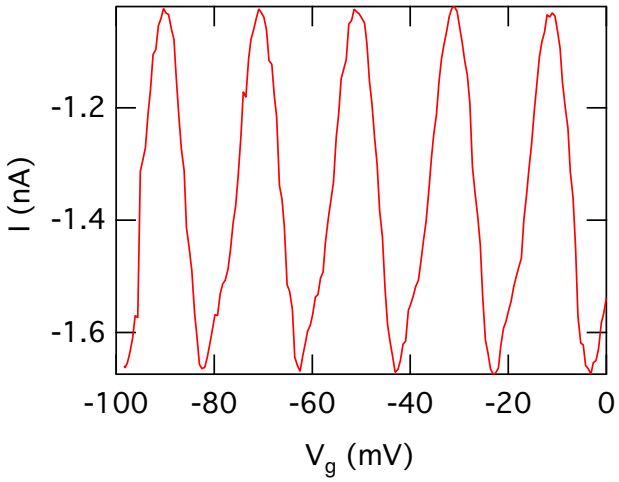

Figure 5.3: Coulomb oscillations of the SET current.

nelings in the stability map [68] are labeled in the figure. Theoretically the Cooper pair peaks should have a $2e$ periodicity. In reality the $2e$ periodicity can be easily destroyed by quasiparticle poisoning. However, with careful design to increase the gap Δ_i, the $2e$ periodicity has been observed[40, 69].

5.2.2 Charge sensing of a QD

Fig. 5.5 is the schematic diagram of a coupled QD-SET system, where C_d is the capacitance between the dot gate and the QD and C_s is the capacitance between the same dot gate to the SET. Meanwhile, the SET and the QD are coupled through C_c. The effective offset charges induced by the gate voltage V_g on the SET Q_{0s} and the

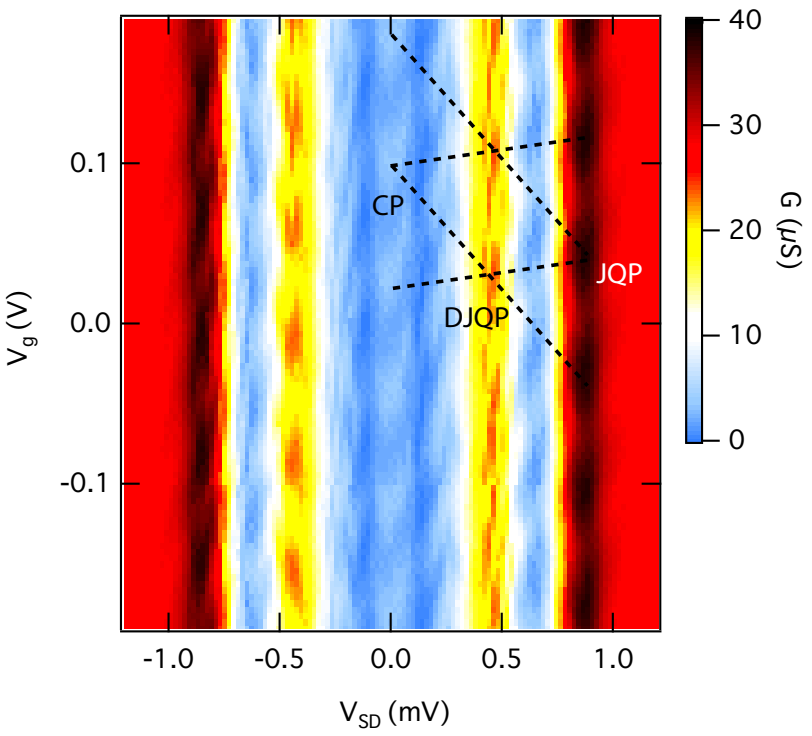

Figure 5.4: Stability diagram of a superconducting SET, showing periodic conductance peaks from CP, DJQP and JQP tunnelings

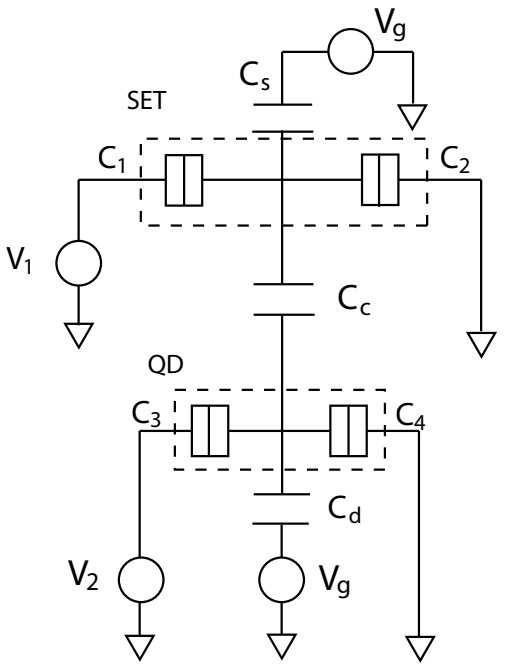

Figure 5.5: A QD-SET system. SET and QD are coupled through C_c.

QD Q_{0d} can be expressed as:

$$Q_{0s} = C_s V_g + (C_d V_g - N_d e)\frac{C_c}{C_{\Sigma d}} \tag{5.4}$$

$$Q_{0d} = C_d V_g + (C_s V_g - N_s e)\frac{C_c}{C_{\Sigma s}} \tag{5.5}$$

where $N_d e$ and $N_s e$ are electron numbers on the island of the QD and the SET, respectively. $C_{\Sigma d} = C_d + C_3 + C_4 + C_c$ and $C_{\Sigma s} = C_s + C_1 + C_2 + C_c$ are their respective total capacitances.

From Eq. 5.4 and 5.5 it is clear that the charge states of both the QD and the SET can be modulated by V_g. On top of that the QD and the SET can affect each other's charge state as well. Therefore, for ideal charge sensing we want $C_s \ll C_d$,

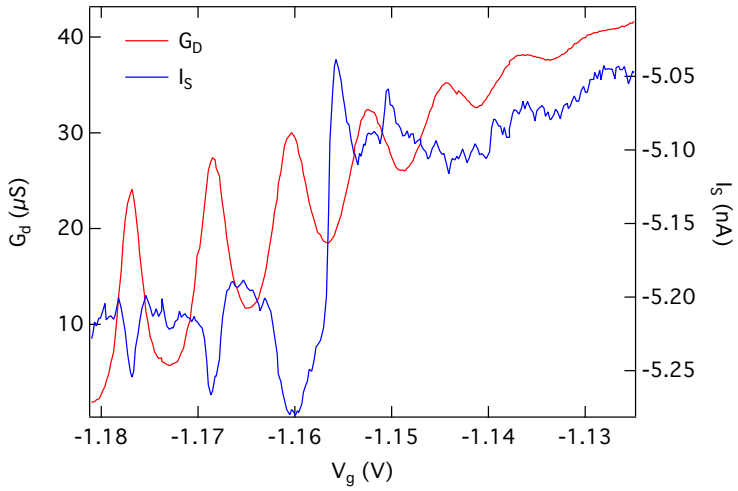

Figure 5.6: Simultaneous measurement of QD conductance G_d and SET current I_s.

in which case the oscillation in SET current caused by direct coupling to V_g will be much slower than the changes caused by the QD.

Fig. 5.6 shows an example of charge sensing. The red curve corresponds to the differential conductance G_d of the QD, showing Coulomb oscillations. The blue curve is the SET dc current. As a result of the coupling between the QD and the SET, as the charge state in the QD is changed by one electron, a sudden change is induced in the SET current. In some cases, G_d becomes too small to be measured but the SET continues to sense charges as demonstrated in Fig. 5.7.

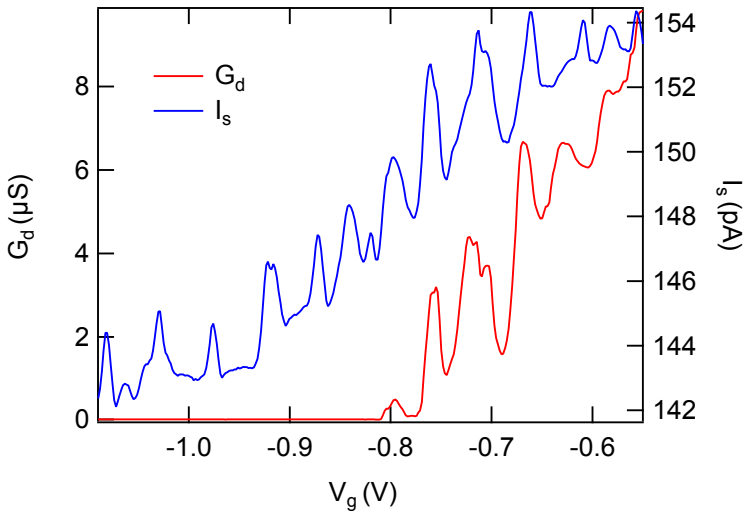

Figure 5.7: Simultaneous measurement of QD conductance G_d and SET current I_s. The SET continues to sense charges in a Regime where G_d becomes too small to measure.

Chapter 6

Real-time charge detection

6.1 Radio-frequency SET

The ability of counting electrons one by one as they tunnel on and off the QD would provide a more direct way of studying single-electron phenomena and offer sophisticated read-out mechanism for quantum control. However it imposes great challenges since electron charges as well as the time scale of electron tunneling are small. As a result, a charge detector with high charge sensitivity and fast response time is desirable.

The superconducting SET, having an ultra high charge sensitivity, is a promising candidate. Nevertheless, the relatively large resistance of the SET R_d greatly limits its detection time. With a typical value of $R_d = 100$ kΩ and the cable capacitance of $C = 1$ nF, the bandwidth of the system is estimated to be $1/(2\pi R_d C) = 1.6$ kHz.

A solution to this problem, the radio-frequency SET (rf-SET), was developed by Schoelkopf *et al.* in 1998. The essence of the rf-SET is impedance matching. The SET

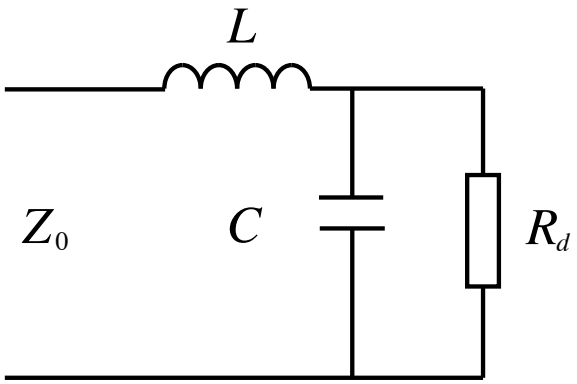

Figure 6.1: Schematic of the resonant circuit

is embedded in a resonant circuit which can be impedance-matched to the standard 50 Ω transmission line. Consider the LCR circuit illustrated in Fig. 6.1. The input impedance is

$$\begin{aligned} Z &= i\omega L + \frac{1}{i\omega C + 1/R_d} \\ &= \frac{R_d}{1+\omega^2 C^2 R_d^2} + i\omega \frac{L - CR_d(1-\omega^2 LC)R_d}{1+\omega^2 C^2 R_d^2}. \end{aligned} \tag{6.1}$$

In order to achieve perfect matching, the following conditions need to be satisfied:

$$\mathrm{Re}[Z(\omega_0)] = Z_0 \tag{6.2}$$

$$\mathrm{Im}[Z(\omega_0)] = 0, \tag{6.3}$$

where ω_0 is the resonant frequency. By solving Eq. 6.3, one arrives at

$$\omega_0 = \frac{1}{\sqrt{LC}} \sqrt{1 - \frac{4C}{R_d^2}}. \tag{6.4}$$

At the resonant frequency ω_0 the input impedance is real and can be solved by substituting Eq. 6.4 in Eq. 6.1:

$$Z(\omega_0) = \frac{L}{CR_d}. \tag{6.5}$$

For perfect matching $\frac{L}{CR_d} = Z_0$ (Eq. 6.2). In reality, to comply with available electronic devices, we want $f_0 = \omega_0/2\pi \approx 1$ GHz. This results in a less-than-perfect matching network. For $f_0 = 1$ GHz and a typical value of the shunt capacitance $C = 0.3$ pF, $L \approx 100$ nH and $\omega_0 \approx \frac{1}{\sqrt{LC}}$. It is convenient to define the unloaded quality factor:

$$Q_0 \equiv \frac{\omega_0 L}{Z_0} = \sqrt{\frac{L}{C}}/Z_0 \tag{6.6}$$

The reflection coefficient is defined as

$$\Gamma \equiv \frac{V^-}{V^+} = \frac{Z - Z_0}{Z + Z_0}. \tag{6.7}$$

Substituting in Eq. 6.5 and 6.6 we get the reflection coefficient Γ_1 for the resonant circuit

$$\Gamma_1 = -1 + \frac{2}{1 + \frac{R_d}{Q_0^2 Z_0}}. \tag{6.8}$$

Without the matching network, the transmission line is directly terminated by the SET and the reflection coefficient Γ_2 is

$$\Gamma_2 = \frac{R_d - Z_0}{R_d + Z_0} = -1 + \frac{2}{1 + \frac{Z_0}{R_d}}. \tag{6.9}$$

Let $Z_0/R_d = x$. Since $x \ll 1$ we can expand Γ_1, Γ_2 as

$$\Gamma_1 = -1 + 2Q_0^2 x \tag{6.10}$$

$$\Gamma_2 = 1 - 2x \tag{6.11}$$

and consequently

$$|\Gamma_1|^2 = 1 - 4Q_0^2 x \tag{6.12}$$

$$|\Gamma_2|^2 = 1 - 4x. \tag{6.13}$$

Therefore, for the same amount of change in R_d, the modulation in the reflected power, which is proportional to $|\Gamma|^2$, will be enhanced by Q_0^2 by the matching network.

6.2 Experimental set-up

6.2.1 Measurement scheme

The sample designs are shown in Fig. 2.6. We use a reflectometry circuit, illustrated by Fig. 6.2. The differential resistance of the SET R_d, an off-chip inductor L and the stray capacitance C to ground form the rf-SET resonant circuit, which is coupled to a QD. We fabricate a superconducting Al spiral inductor to avoid introducing extra loss. The SET is internally grounded by directly wire-bonding the SET drain to the ground plane. The sample is mounted in the ^{3}He refrigerator with a base temperature of 0.3 K. A carrier wave at the resonant frequency is fed into the rf-SET from the coupling terminal of the directional coupler. The charge state in the QD shifts the

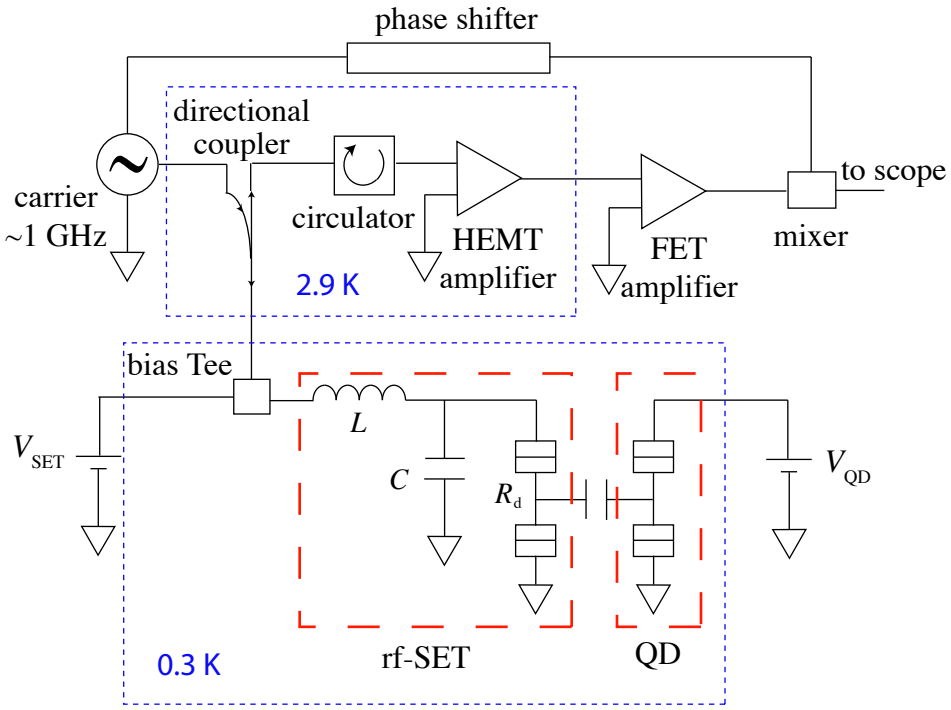

Figure 6.2: Circuit diagram for the real-time measurement

offset charges in the SET and subsequently R_d. When the time scale of electron tunneling falls within the detection bandwidth of the rf-SET, fast read-out of the charge state can be realized. The reflected signal of the rf-SET, carrying information about the QD charge state, is amplified by a high electron mobility transistor (HEMT) amplifier at 2.9 K after passing through the directional coupler and the circulator that prevents the noise generated by the amplifier from entering the rf-SET. At room temperature, the signal is further amplified by a field effect transistor (FET) amplifier before it is demodulated by a mixer. Eventually the real-time signal is recorded by a digital oscilloscope (TDS7704B).

A double-balance mixer (model ZMF-2000 by Mini-Circuit) is used to demodulate

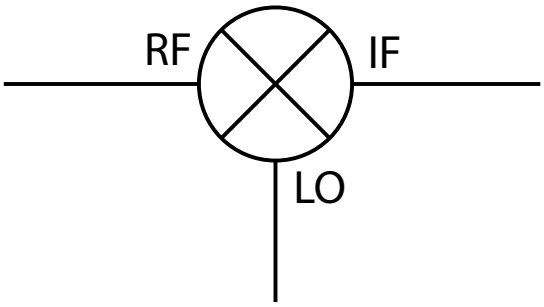

Figure 6.3: Schematic of a mixer

the reflected signal. As illustrated in Fig. 6.3, a mixer has three ports, namely the local oscillation (LO), the RF and the intermediate frequency (IF) port. Following Ref.[70], the reflected signal modulated by the QD charge state, sent into the RF port can be expressed as

$$v(t) = v_0(1 + m\cos\omega_m t)\cos\omega_0 t, \tag{6.14}$$

where the modulation frequency ω_m is much smaller than the resonant frequency ω_0 and m is the modulation depth ($0 \leq m \leq 1$). The LO port is connected to a signal generated at the carrier wave frequency ω_0:

$$v_l(t) = v_1\cos(\omega_0 t + \phi) \tag{6.15}$$

In the actual experiment, we use two separate but phase-locked signal generators for the carrier wave sent into the rf-SET and the signal for the LO port. By doing this instead of using a power splitter, we can easily adjust the power of the two waves individually.

The IF port output is the product of $v(t)$ and $v_l(t)$. By substituting in Eq. 6.14

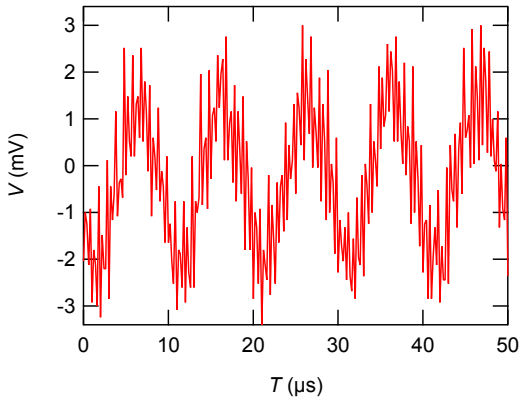

Figure 6.4: Demodulated gate signal

and Eq. 6.15, we can express the output signal as

$$\begin{aligned} v_{out} &= v(t) \times v_l(t) \\ &= \frac{v_0 v_1}{2}(1 + m\cos\omega_m t)\cos(2\omega_0 t + \phi) \\ &+ \frac{v_0 v_1}{2}(m\cos\phi\cos(\omega_m t) + \cos\phi) \end{aligned} \tag{6.16}$$

A low-pass filter can be used to filter away the first term at the frequency of $2\omega_0$. In the experiment we use a 2 MHz low pass filter. The remaining term recovers the modulating signal at ω_m with modulation depth m. It is usually necessary to tune the phase shift ϕ to be equal to $n\pi$ to achieve maximum signal amplitude, which is achieved by the phase shifter in Fig. 6.2.

To verify that the mixer functions properly, we apply a small excitation at 100 kHz on the SET's own gate, corresponding to 0.012 e modulation of the offset charges. The carrier wave is at the resonant frequency of the rf-SET, 936 MHz. Fig. 6.4 shows the output of the mixer recorded by the oscilloscope, recovering the modulation signal at 100 kHz.

6.2.2 Attenuation and amplification

The input coaxial line includes attenuation of 34 dB to help achieve the desired small carrier wave amplitude and amplifiers are used at the output to acquire measurable signals. The HEMT amplifier, mounted on the pulse tube cooler (PTC) 2nd stage, amplifies the signal by about 25 dB at 2.9 K and the FET amplifier at room temperature adds another 40 dB.

To verify the noise added by the amplifiers we measure the noise spectrum of the output signals. The SET is biased at the normal conductance regime and we send in a carrier wave of -54 dBm at $f_0 = 892$ MHz. In Fig. 6.5 the green curve represents the noise floor of the oscilloscope used to measure the real-times signal. The bandwidth from dc to 2 MHz is defined by the low-pass filter at the output. The red curve corresponds to the noise spectrum when the FET amplifier is turned on, adding about 6 dB to the noise floor and finally the HEMT amplifier is also turned on, resulting in the black curve. The whole chain of amplifiers add a total of about 18 dB to the noise floor of the oscilloscope and from Fig. 6.5 we can see that the major source of noise is the cold HEMT amplifier.

6.2.3 Calibration of the rf-SET

A network analyzer that simultaneously measures the reflection coefficient over a specified frequency range is used to locate the resonant frequency $f_0 = \omega_0/2\pi$ of the rf-SET. As discussed in Section 6.1, the reflection coefficient Γ is modulated by the SET differential resistance R_d. One example is demonstrated in Fig. 6.6. Fig. 6.6(a) shows the superconducting I-V curve of an rf-SET with clear superconducting gap. The reflection coefficient Γ is plotted in Fig. 6.6(b), where different curves corresponding

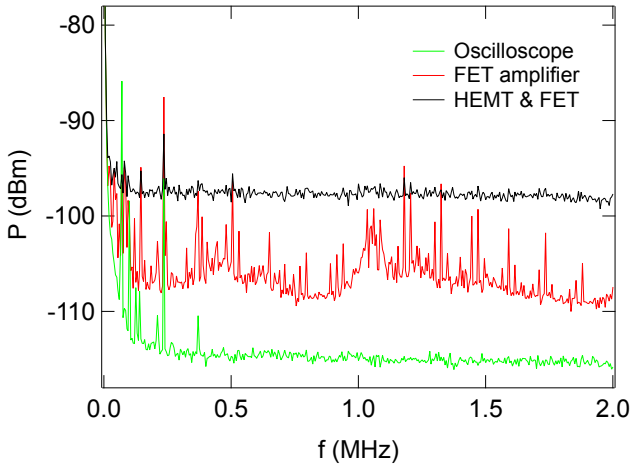

Figure 6.5: Noise spectrum of the amplifiers

to different R_d, indicating a resonant frequency of 883 MHz. The legend indicates the corresponding dc bias applied on the SET. Tracing the superconducting I-V curve of the SET in Fig. 6.6(a), we can see that R_d can be changed by the bias voltage. Within the superconducting gap $R_d \rightarrow \infty$ and most of the power is reflected (black curve). When R_d becomes finite good matching can occur and the power is dissipated in the rf-SET, resulting in a dip in Γ at the resonant frequency f_0 as indicated by the blue and red curves.

In what follows we will calibrate the charge sensitivity δq of the rf-SET. First we measure the coulomb oscillations of the SET by recording the dc current in the sub-gap regime while sweeping the SET gate, as shown in Fig. 5.3 and determine the gate voltage that corresponds to one electron cycle. Then a carrier wave at f_0 is sent into the rf-SET. Meanwhile, a small ac signal at 100 kHz, corresponding to a fraction of an electron cycle q_0 is applied to the SET gate. The spectrum of the reflected power is measured by a spectrum analyzer, which shows a major peak at f_0 and two

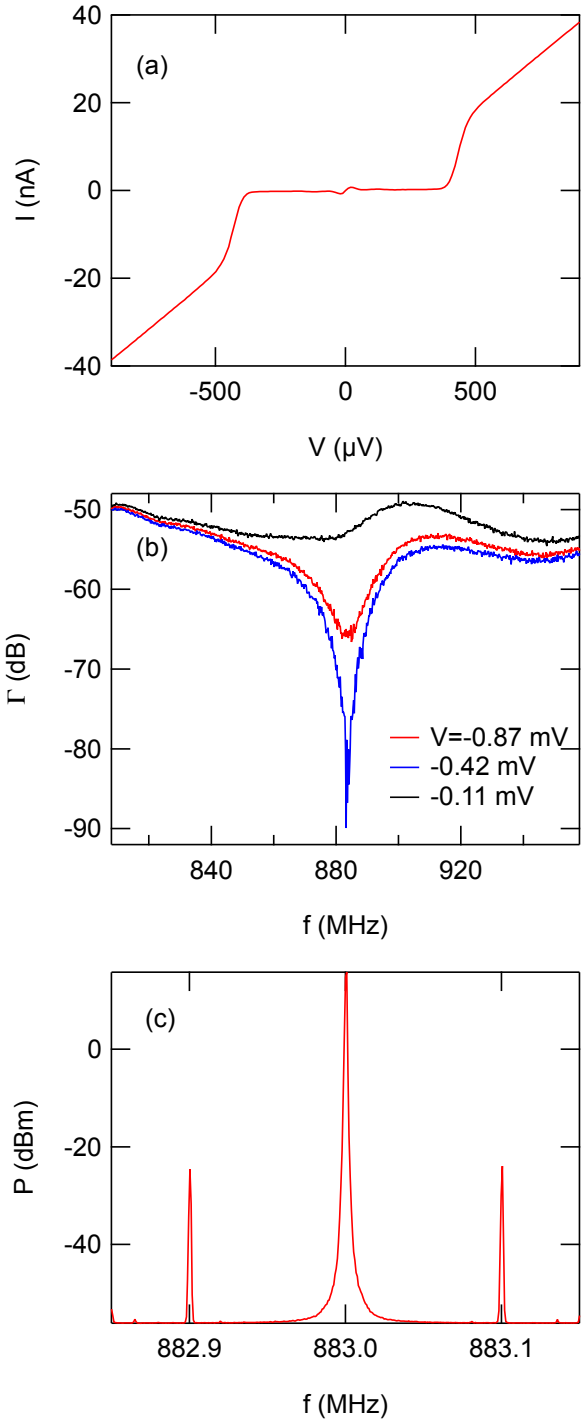

Figure 6.6: Calibration of an rf-SET

side peaks 100 kHz away from f_0 as a result of the modulation from the gate. The charge sensitivity δq can be determined by the signal-to-noise ratio (SNR) of the side peaks with

$$\delta q = \frac{q_0}{\sqrt{2B}10^{\mathrm{SNR}/20}}, \tag{6.17}$$

where B is the resolution bandwidth and the SNR is in dB. In Fig. 6.6(c) SNR= 32 dB, the gate excitation corresponds to $q_0 = 0.015\ e$ and the resolution bandwidth of the spectrum analyzer is set to be 1 kHz. From Eq. 6.17 the charge sensitivity is calculated to be $8 \times 10^{-6} e/\sqrt{\mathrm{Hz}}$.

6.3 Real-time results

6.3.1 Read-out of electron tunneling

Although the intrinsic bandwidth of the rf-SET can reach 100 MHz, in practice the detection bandwidth is limited by noise and weak coupling to the QD. We therefore use a 2 MHz low pass filter at the output and focus on time scales longer than microseconds. A change in the QD occupancy by one electron manifests itself as switching between two levels in the time domain resembling a random telegraph signal (RTS), which is what we observe when all three dot gates are sufficiently energized. An example of such switching is shown in Fig. 6.7 for an rf-SET with $\delta q = 4 \times 10^{-6} e/\sqrt{\mathrm{Hz}}$. Fig. 6.7(a) corresponds to point A in the QD transport current (Fig. 6.7(d)), in which the lower level, i.e. the (N) electron state in Fig. 6.7(d) is more stable, with occasional upward transitions to the $(N+1)$ state. At point B the two charge states are degenerate so the dwell times of each level are comparable, as shown in Fig. 6.7(b). At point C the $(N+1)$ state becomes more probable, as

demonstrated in Fig. 6.7(c).

We can open up the QD by reducing the voltage applied on the gates. As the tunnel barriers become more transparent the timescale of the switching events reduces, as shown in Fig. 6.8. This rf-SET can resolve RTS with a resolution of 10 μs, demonstrating its ability to perform fast charge sensing. The minimum detection time t_m in real-time measurement can be estimated as [71]

$$t_m \approx 8(\frac{\delta q}{\kappa e})^2, \tag{6.18}$$

where κe $\sim$0.01e is the shift in rf-SET's polarization charge due to a change of one electron in the QD charge state. The lower bound of t_m is estimated to be in the microsecond range. When charge sensing the QD, δq usually does not reach the optimal value quoted above and the detection time we observe is reasonable.

6.3.2 Spectral analysis

A fast Fourier transform (FFT) can be applied on the RTS data to obtain the spectrum, from which the total tunneling rate $\Gamma = \Gamma_0 + \Gamma_1$ can be extracted. The respective tunneling rates correspond to $\Gamma_0 = \tau_0^{-1}$ and $\Gamma_1 = \tau_1^{-1}$, where $\tau_{0,1}$ are the mean times spent in each state.

Fig. 6.9 shows the power spectra of the rf-SET output near two different charge degeneracy points fit to a Lorentzian function (blue lines). In Fig. 6.9(a) the value of the total tunneling rate is extracted to be $\Gamma = 2.24 \times 10^2$ s^{-1} and for Fig. 6.9(b) $\Gamma = 3.16 \times 10^3$ s^{-1}.

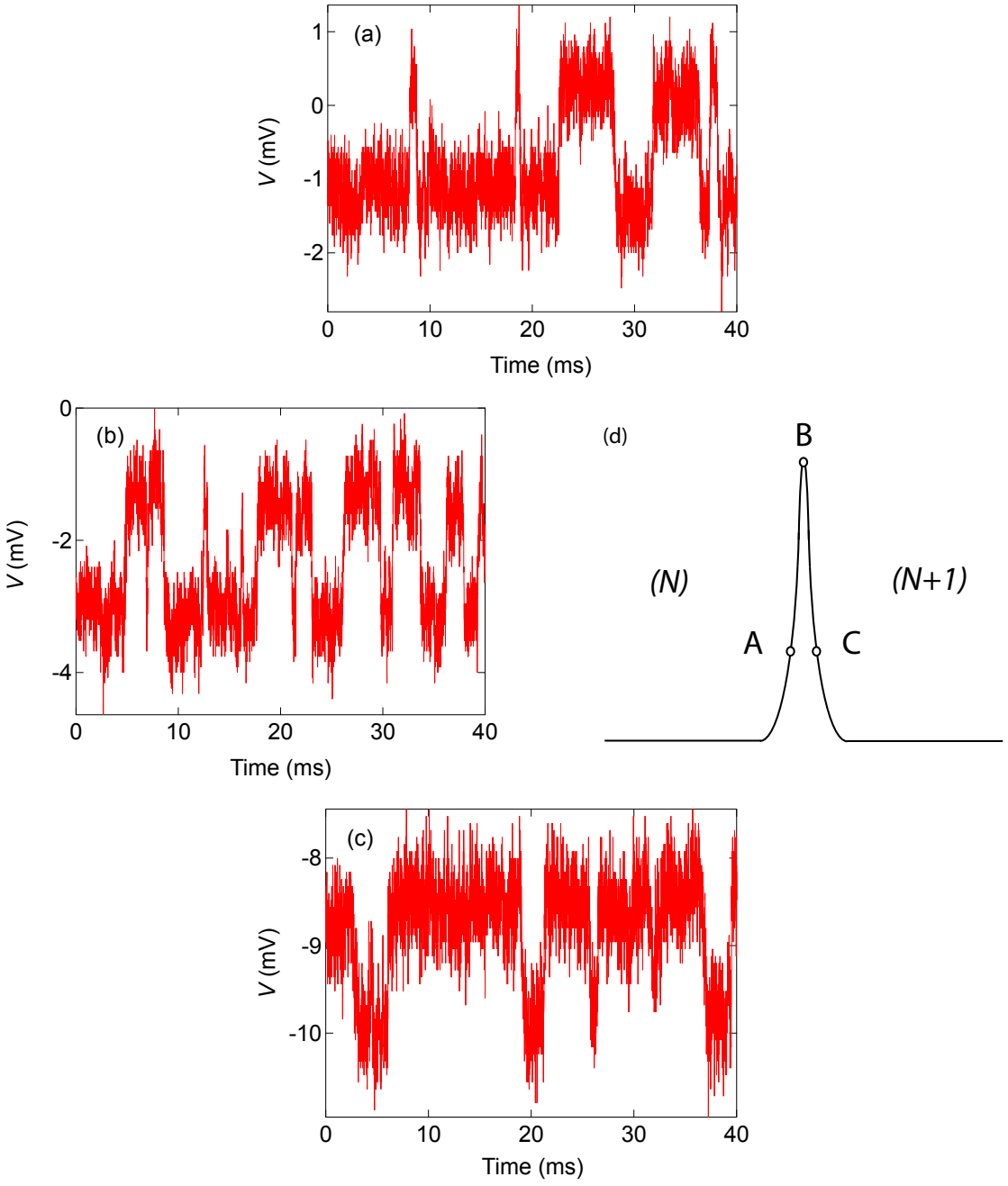

Figure 6.7: Representative real-time output of an rf-SET reading out the change of a charge state in the QD.

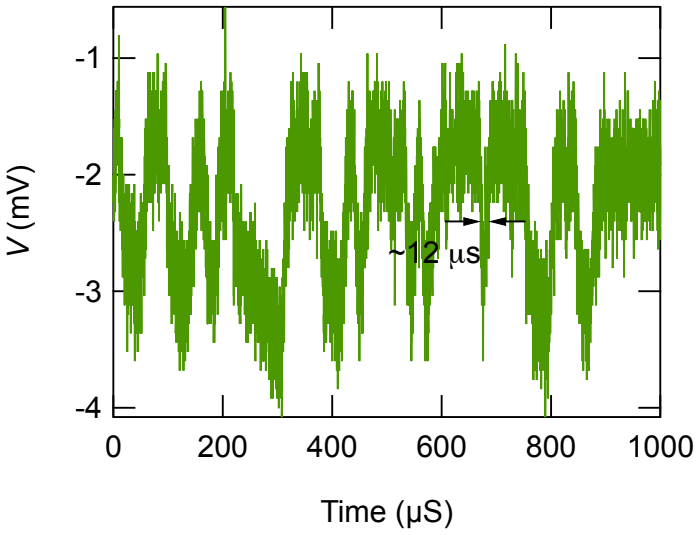

Figure 6.8: The minimum charge detection time of this rf-SET is on the order of 10 μs.

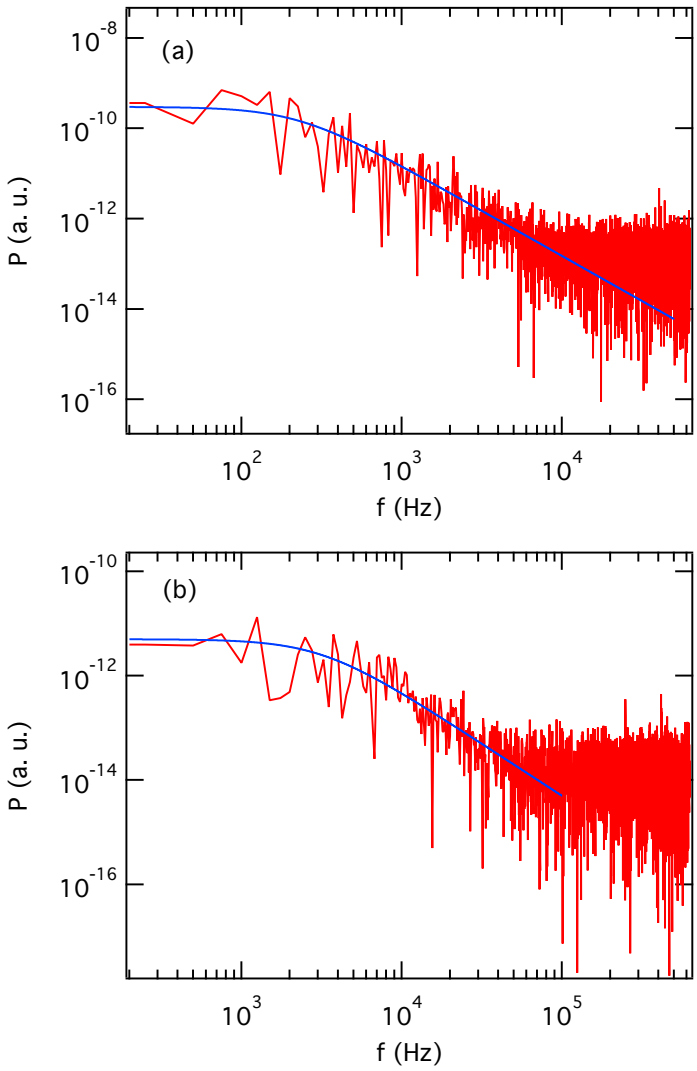

Figure 6.9: FFT spectra of the rf-SET real-time output near two different charge degeneracy points

Chapter 7

Double quantum dot charge sensing

7.1 Classical theory for double quantum dots

When two single QDs are coupled to each other, they form a double quantum dot (DQD) system. In this introduction we ignore the energy quantization in the QDs, resulting in a purely classical description of single-electron phenomena. Following the method in [72] we can model the DQD as shown in Fig. 7.1.

The charge and potential on dot 1(2) are $Q_{1(2)}$ and $V_{1(2)}$. Each dot is coupled to a gate voltage $V_{1(2)}$ through a capacitor $C_{g1(2)}$. The two dots are coupled to each other via a capacitor C_m and the whole DQD is coupled to the source (drain) voltage $V_L(V_R)$ via the capacitor $C_L(C_R)$. The total charges $Q_{1(2)}$ on dot 1(2) can be written as

$$Q_1 = C_L(V_1 - V_L) + C_{g1}(V_1 - V_{g1}) + C_m(V_1 - V_2) \tag{7.1}$$

$$Q_2 = C_R(V_2 - V_R) + C_{g2}(V_2 - V_{g2}) + C_m(V_2 - V_1), \tag{7.2}$$

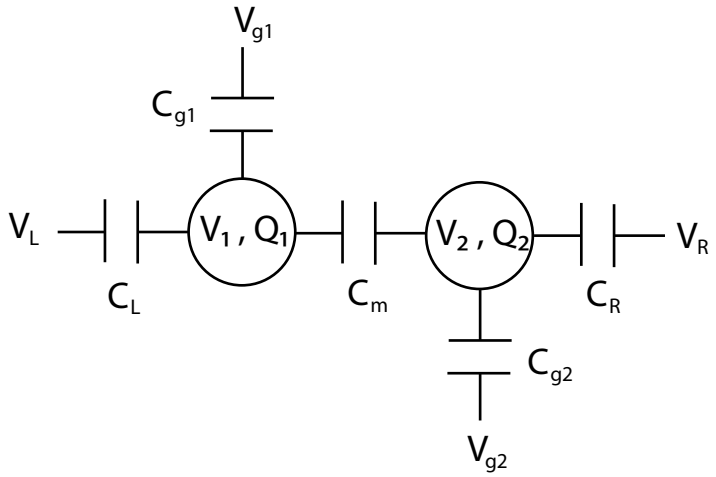

Figure 7.1: Model of a DQD system.

which can also be rearranged in the vector form as

$$Q_{eff} = \begin{pmatrix} Q_1 + C_L V_L + C_{g1} V_{g1} \\ Q_2 + C_R V_R + C_{g2} V_{g2} \end{pmatrix} = \begin{pmatrix} C_1 & -C_m \\ -C_m & C_2 \end{pmatrix} \begin{pmatrix} V_1 \\ V_2 \end{pmatrix}, \tag{7.3}$$

where $C_1 = C_L + C_{g1} + C_m$ and $C_2 = C_R + C_{g2} + C_m$. We can rewrite Eq. 7.3 as

$$\overrightarrow{Q}_{eff} = \mathbf{C}_{cc} \cdot \overrightarrow{V}, \tag{7.4}$$

with the capacitance matrix $\mathbf{C}_{cc} = \left(\begin{smallmatrix} C_1 & -C_m \\ -C_m & C_2 \end{smallmatrix} \right)$ and the voltage vector $\overrightarrow{V} = \left(\begin{smallmatrix} V_1 \\ V_2 \end{smallmatrix} \right)$.

The electrostatic energy is given by

$$U = \frac{1}{2} \overrightarrow{V} \cdot \overrightarrow{Q}_{eff} = \frac{1}{2} (\mathbf{C}_{cc}^{-1} \cdot \overrightarrow{Q}_{eff}) \cdot \overrightarrow{Q}_{eff}. \tag{7.5}$$

Rewriting $Q_{1(2)}$ as $Q_{1(2)} = -eN_{1(2)}$, U becomes a function of N_1 and N_2, i. e.

$U(N_1, N_2)$, where $N_{1(2)}$ is the number of electrons in dot 1(2). The electrochemical potential $\mu_{1(2)}(N_1, N_2)$ of each dot, defined as the energy required to add the $N_{1(2)}$th electron to dot 1(2), can be expressed as

$$\mu_1(N_1, N_2) \equiv U(N_1, N_2) - U(N_1 - 1, N_2) \tag{7.6}$$

$$\mu_2(N_1, N_2) \equiv U(N_1, N_2) - U(N_1, N_2 - 1) \tag{7.7}$$

Let $V_R = 0$ and $V_L = V$. In the V_{g1}, V_{g2} plane, borders of charge stability regions are defined by the following groups of lines:

$$\mu_1(N_1 + 1, N_2) = -eV \tag{7.8}$$

$$\mu_2(N_1, N_2 + 1) = 0 \tag{7.9}$$

$$\mu_1(N_1 + 1, N_2) = \mu_2(N_1, N_2 + 1). \tag{7.10}$$

7.1.1 Linear transport regime

We first consider the linear transport regime, in which $V \approx 0$. We construct the charge stability diagram, commonly known as the honeycomb diagram with Eq. 7.8-7.10 in Fig. 7.2, using the following parameters: $C_1 = 80$ aF, $C_2 = 60$ aF, $C_{g1} = 10$ aF and $C_{g2} = 2.4$ aF while varying the value of C_m.

When $C_m \ll C_1, C_2$, the two dots are mostly decoupled, and the system behaves like two single dots. As shown in Fig. 7.2(a) corresponding to $C_m = 2$ aF, the red lines separate the different charge states in dot 1 and the blue lines separate the different charge states in dot 2. V_{g1} and V_{g2} control the charge states in dot 1 and 2 respectively, with little effect on the other dot, as demonstrated by the approximately

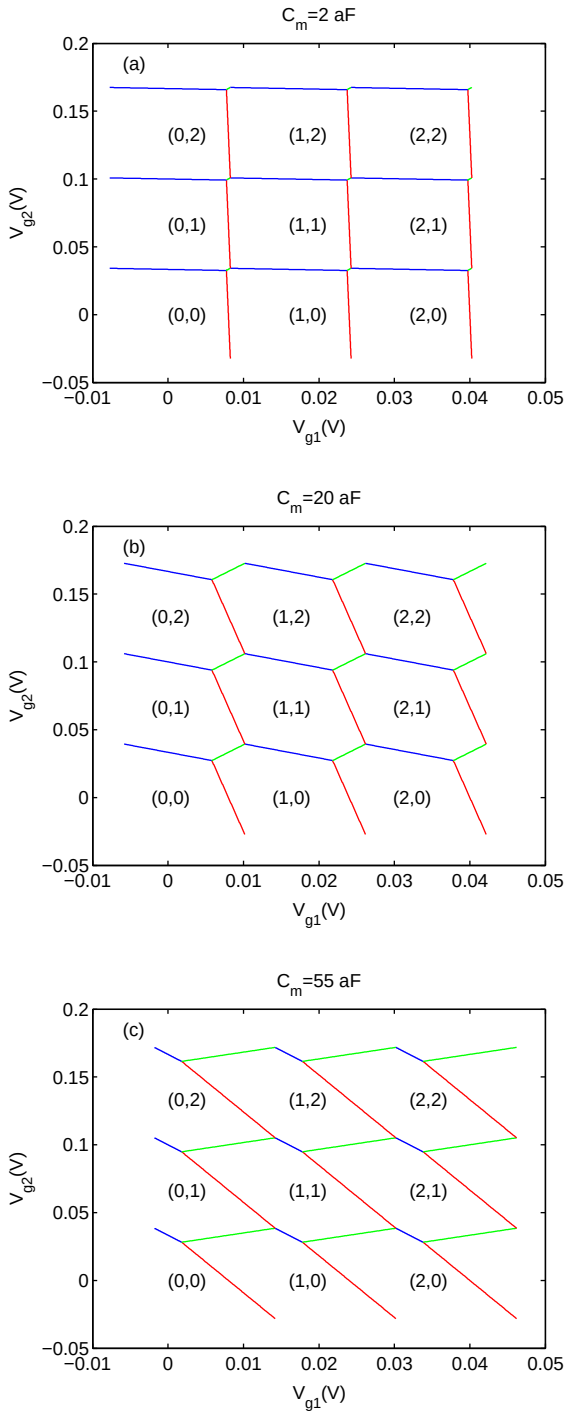

Figure 7.2: Simulated stability diagram of a DQD system with (a) small, (b) intermediate and (c) large interdot coupling

vertical red lines and the approximately horizontal blue lines. The charge states are labeled with (N_1, N_2). As C_m increases, the two dots begin to couple to each other and the honeycomb structure appears (Fig. 7.2(b)). The intersection of the four neighboring charge states separate into triple points, connected by the green lines as shown in Fig. 7.2(b) where $C_m = 20$ aF. If the DQD is sufficiently isolated from the leads, triple points become the only places where detectable charge transitions can occur, since edges of the honeycombs are only visible due to co-tunneling processes. As C_m increases further and approaches C_1, C_2, the DQD is equivalent to one big single QD and the charge states are better described by $N = N_1 + N_2$ instead of N_1 and N_2 individually. In Fig. 7.2(c) we simulate the stability diagram for $C_m = 55$ aF. It can be seen that the honeycombs transform into regions between parallel lines, typical for a single QD controlled by two gates.

7.1.2 Nonlinear transport regime

We now introduce a non-zero bias V. By solving Eq. 7.8- 7.10, we can again simulate the stability diagram. The results for $V = 0.5$ mV and $V = -0.5$ mV are shown in Fig. 7.3(a) and (b), respectively. The capacitances are the same as in Fig. 7.2(b). It can be seen that triple points expand into triangles in the presence of a bias voltage. Bias voltages of different signs result in triangles with 180°-rotated orientations. It is worth noticing that the triple points expand in all directions as V is increased and all three groups of lines, each group with a different slope, are shifted. The relative positions of the positive-bias triangles, the triple points at zero bias, and the negative-bias triangles are demonstrated in Fig. 7.3(c).

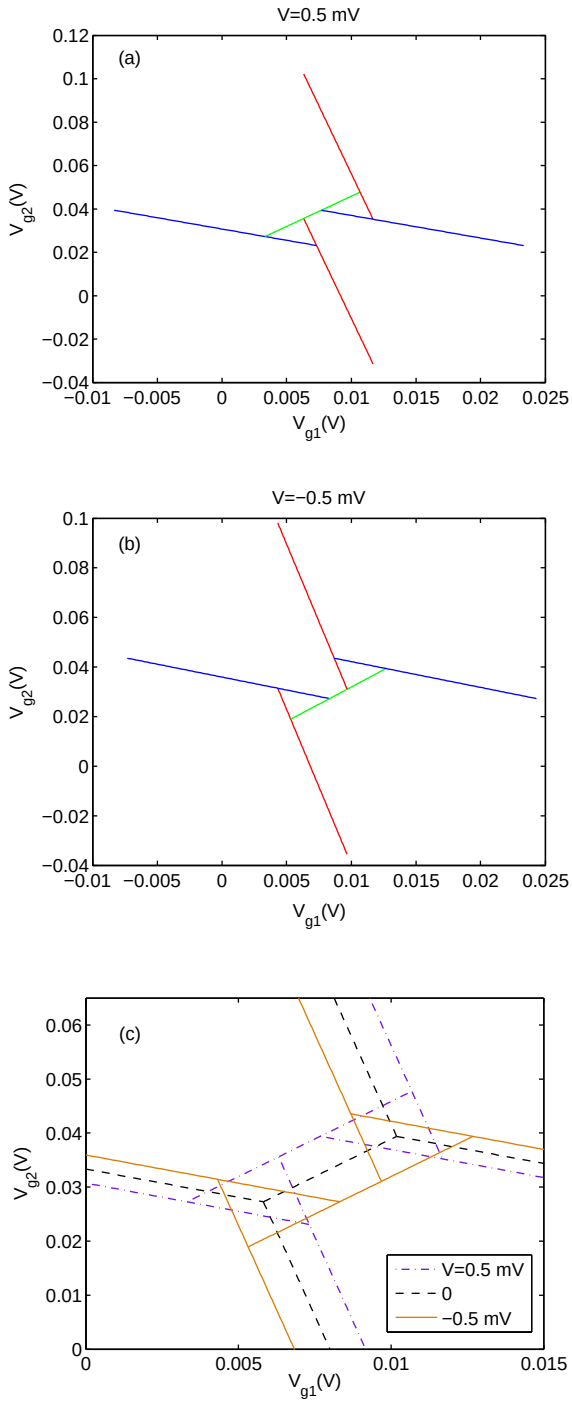

Figure 7.3: Simulated bias triangles for (a) $V > 0$, (b) $V < 0$ and (c) both $V > 0$ and $V < 0$ together with $V = 0$.

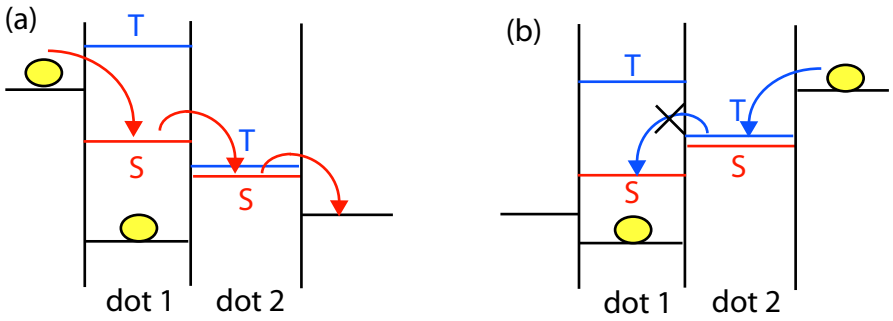

Figure 7.4: Schematic illustration of Pauli spin blockade. The red(blue) lines labeled with S(T) represent the singlet(triplet) states. The singlet and triplet states in dot 2 are nearly degenerate due to weak interdot tunnel coupling.

7.2 Pauli spin blockade

In DQD the effect of Pauli spin blockade can appear when an energetically favorable state cannot be accessed due to spin conservation, preventing charge transitions through the DQD from happening [73, 74, 75, 76, 77, 78, 79, 80]. In the case of the $(N_1, N_2) = (2, 0) \rightarrow (1, 1)$ transition, when the left lead is negatively biased, corresponding to Fig. 7.4(a), an electron entering dot 1 forming a (2,0) singlet can exit through the (1,1) singlet state. The singlet and the triplet states of (1,1) are nearly degenerate due to weak interdot tunneling [81]. At positive bias illustrated in Fig. 7.4(b), an electron can enter dot 2 to form a (1,1) triplet state. Exit through (2,0) singlet state is forbidden due to spin conservation and transition is blockaded. This asymmetry of negative and positive biases results in current rectification.

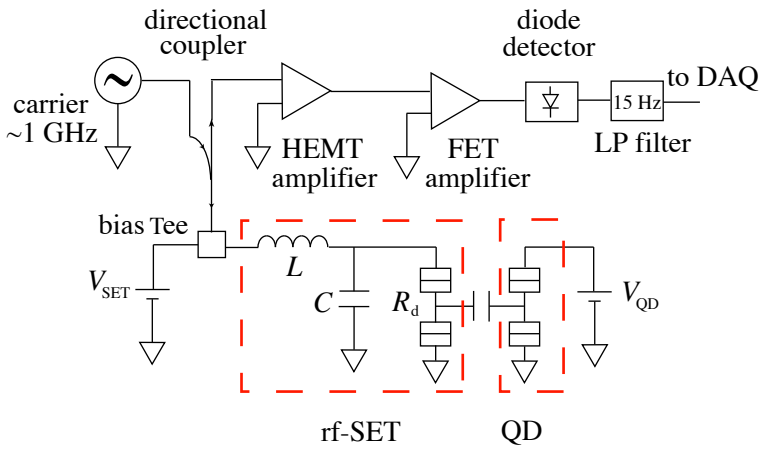

Figure 7.5: Circuit diagram for DQD charge sensing

7.3 Experimental result

7.3.1 Measurement set-up

In this sample, an rf-SET with a charge sensitivity of $5 \times 10^{-5}\ e/\sqrt{\text{Hz}}$ is coupled to a DQD. In this case, the best possible detection time is about 200 μs, which makes it very difficult for the rf-SET to perform real-time measurement, so the reflected signal is demodulated by a diode detector and averaged by a 15 Hz low-pass (LP) filter. The sample is measured at a temperature of 0.3 K. Fig. 7.5 is a schematic diagram of the measurement circuit.

We form a DQD with gates 1-4 (see Fig. 2.6(c)). Voltages V_{g3} and V_{g4} are kept constant, while V_{g1}, V_{g2} control the left and right dots respectively. The stability diagram of a nearly uncoupled DQD is plotted in Fig. 7.6(a) and (b). In Fig. 7.6(a) the differential conductance G is taken with lock-in measurement. In Fig. 7.6(b) the

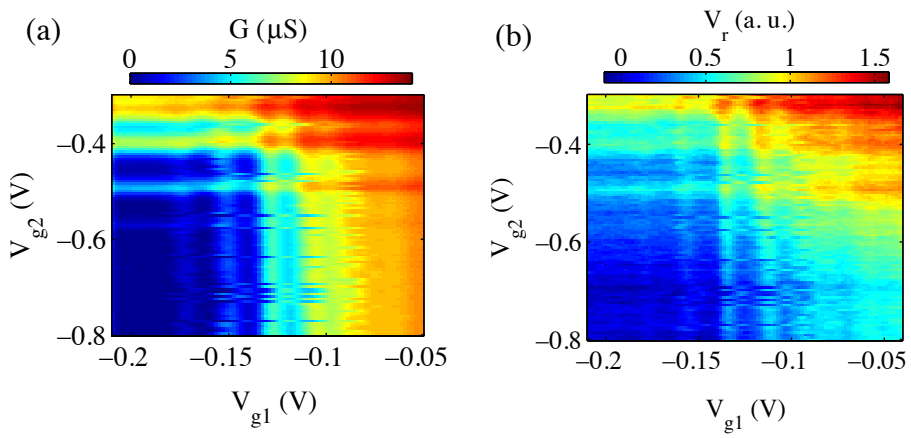

Figure 7.6: Stability diagram of a nearly uncoupled DQD taken with (a) lock-in and (b) rf-SET

reflected signal of the rf-SET is plotted. The results taken with the two methods are comparable.

7.3.2 Measurement of stability diagram in reality

Fig. 7.7 shows the stability diagram of a coupled DQD at approximately zero bias mapped out by the rf-SET. The transport through the DQD is too resistive ($> 1\text{M}\Omega$) for a reliable lock-in measurement. The color scale represents the level of the reflected power, converted into voltage V_r. The characteristic honeycomb-shaped charge stability diagram of a DQD with multiple pairs of triple points can be seen. However, upon careful comparison, there is a significant discrepancy between the simulated Fig. 7.2(b) and Fig. 7.7. In Fig. 7.2(b), the centers of the green lines, i. e. the centers of each pair of triple points, are align in a rectangular grid. In Fig. 7.7 the grid is not rectangle anymore but clearly tilted. This distortion suggests that there is direct

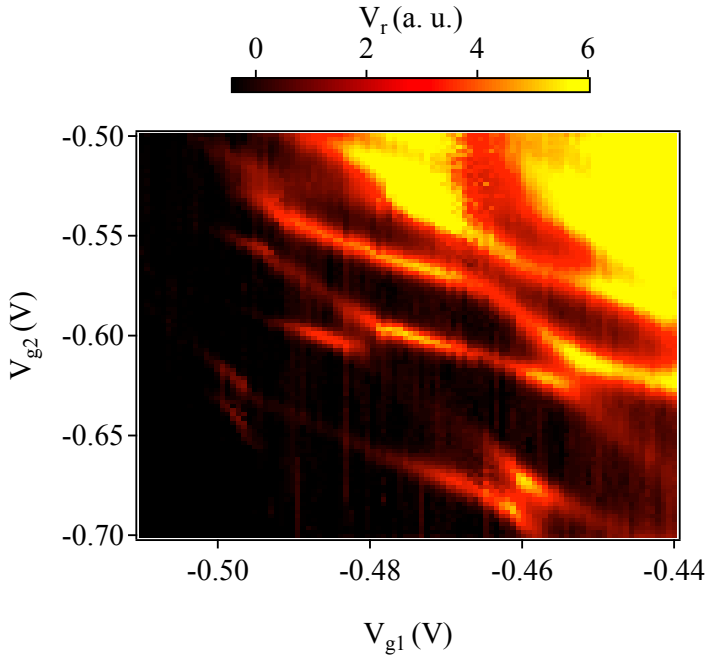

Figure 7.7: Honeycomb diagram of the DQD measured by the rf-SET

coupling between dot 1 and gate 2 (as well as between dot 2 and gate 1) that is ignored by the simplified model in Fig. 7.1.

We can add in a cross-coupling capacitance C_a between dot 1 and gate 2 as well as C_b between dot 2 and gate 1, as illustrated in Fig. 7.8. Correspondingly, Eq. 7.3 is modified as

$$Q_{eff} = \begin{pmatrix} Q_1 + C_L V_L + C_{g1} V_{g1} + C_a V_{g2} \\ Q_2 + C_R V_R + C_{g2} V_{g2} + C_b V_{g1} \end{pmatrix} = \begin{pmatrix} C_1 & -C_m \\ -C_m & C_2 \end{pmatrix} \begin{pmatrix} V_1 \\ V_2 \end{pmatrix}, \tag{7.11}$$

where $C_1 = C_L + C_{g1} + C_m + C_a$ and $C_2 = C_R + C_{g2} + C_m + C_b$. Using the same parameters as in Fig. 7.2(b) together with $C_a = 1.7$ aF and C_b=3.7 aF, we can simulate the modified stability diagram as shown in Fig. 7.9. It is clear that the grid

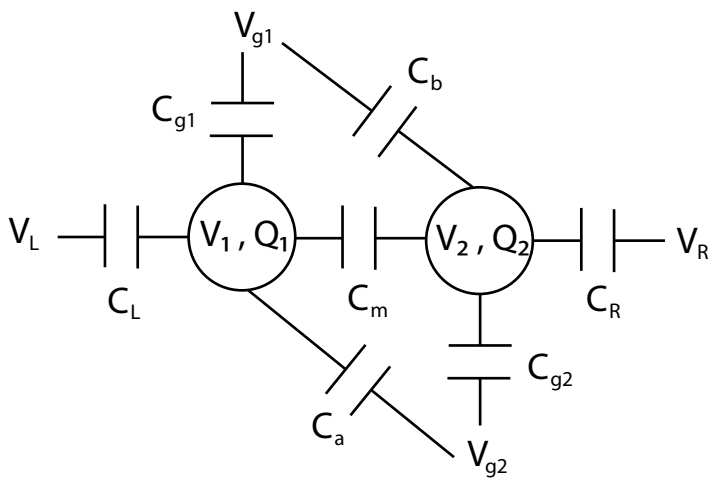

Figure 7.8: An improved model for the DQD system, including cross coupling between dot 1(2) and gate 2(1)

of triple points is now tilted, resembling the experimental data in Fig. 7.7, which verifies that the model including C_a and C_b is more accurate in describing our DQD system.

As we increase the bias voltage, the triple points expand into triangles as shown in Fig. 7.10, where the DQD is biased at $V = -0.6$ mV. Superimposed on the data are the approximate boundaries of the bias triangles. With Fig. 7.7 and Fig. 7.10 we can retrieve the approximate values of the capacitances listed in Table. 7.1. Data in Fig. 7.7 and Fig. 7.10 are taken in 17 min and 10 min respectively at a rate of 10 points per second, approximately 10 times faster than lock-in measurements. Even without real-time detection, the rf-SET can be used to replace lock-in measurement of dot current, greatly reducing the time required for data acquisition.

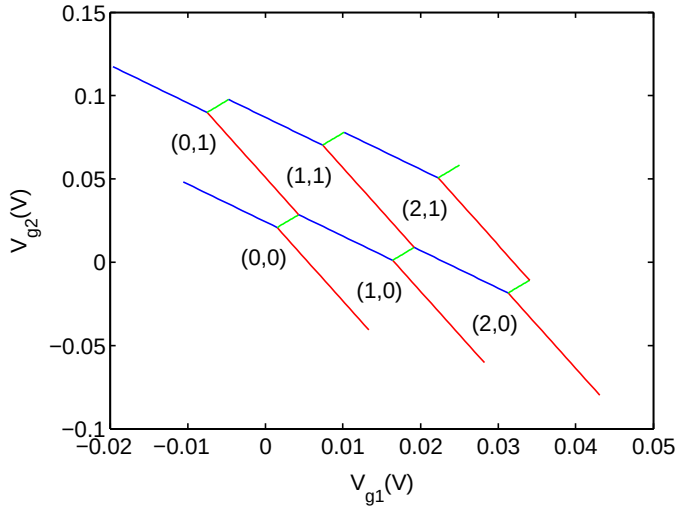

Figure 7.9: Simulated stability diagram using the model illustrated in Fig. 7.8

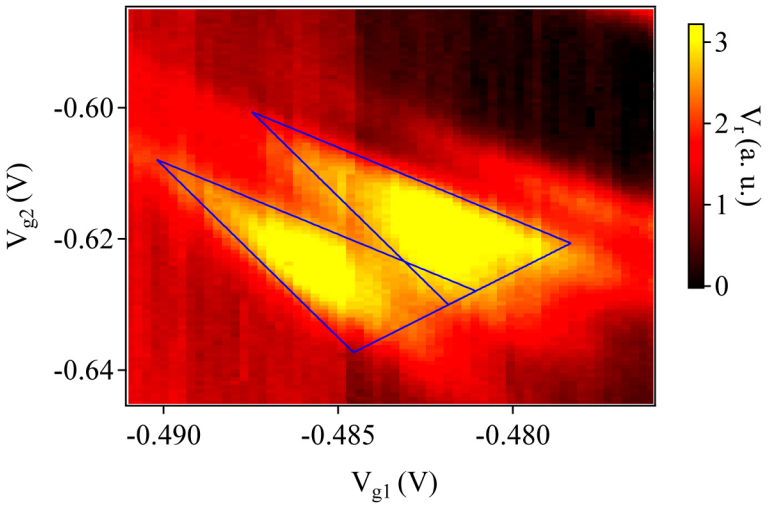

Figure 7.10: Bias triangles for (2.0), (1,1) transition at $V = -0.6$ mV. Superimposed are the approximate boundaries of the triangles that are used to extract the values of the capacitances.

Table 7.1: Subtracted values of capacitances in aF

C_1	C_2	C_{g1}	C_{g2}	C_a	C_b	C_m
141	104	13	2.8	1.7	3.7	38

7.3.3 Spin blockade and excited state transition in Si/SiGe DQD

When a positive bias is applied on the DQD, we see signature of spin blockade. In Fig. 7.11 where $V = 0.4$ mV, the enhanced triangle region is clearly missing other than the edges. This agrees with the picture of Pauli spin blockade illustrated in Fig. 7.4.

In addition, there is another interesting feature in Fig. 7.10. Apart from the pair of triangles superimposed with the blue lines, there is a less bright but clearly enhanced region that is slightly offset. This is most likely due to transition through an excited state in the DQD. In order to understand this qualitatively we modify Eq. 7.8- 7.10 by including the excitation energy $\Delta_{1(2)}$ in dot 1(2).

$$\mu_1(N_1 + 1, N_2) + \Delta_1 = -eV \tag{7.12}$$

$$\mu_2(N_1, N_2 + 1) + \Delta_2 = 0 \tag{7.13}$$

$$\mu_1(N_1 + 1, N_2) + \Delta_1 = \mu_2(N_1, N_2 + 1) + \Delta_2. \tag{7.14}$$

In Fig. 7.12 we compare the original bias triangle data to a fit. Fig. 7.12(a) is identical to Fig. 7.10. Fig. 7.12(b), which has the same scale with Fig. 7.12(a) include two sets of triangles. The blue ones are the ground state triangles generated with

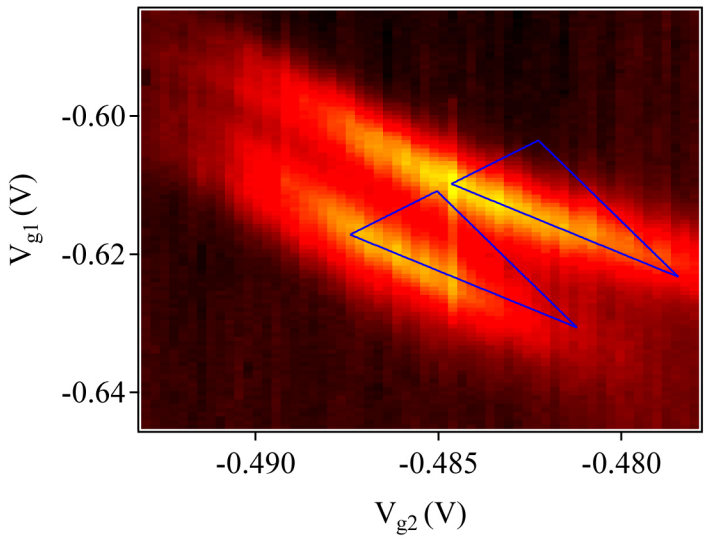

Figure 7.11: For $V = 0.4$ mV the signal in the triangle region is suppressed, indicating spin blockade.

Eq. 7.8- 7.10 and the red ones are excited state triangles generated with Eq. 7.12- 7.14, using $\Delta_1 = 0.4$ meV and $\Delta_2 = 0.25$ meV. To demonstrate the effect of Δ_1 and Δ_2 respectively, we further generate Fig. 7.13, in which the green triangles correspond to $\Delta_1 = 0.4$ meV, $\Delta_2 = 0$ and the magenta triangles correspond to $\Delta_1 = 0$, $\Delta_2 = 0.25$ meV. It can be clearly seen that Δ_1 preserves the lines that define the charge states in dot 2 while Δ_2 preserves the lines that define the charge states in dot 1, in agreement with our model.

Additional enhanced regions are commonly interpreted as triplet triangles [77, 79, 82] which appear when the dc bias exceeds the singlet-triplet splitting in dot 1. This feature is especially significant in Si/SiGe QDs [82] and is considered as an evidence of the long spin relaxation time in Si. However, we conclude that the excited state triangles we observe are not due to triplet states. The reason is that the singlet and triplet states in dot 2, i.e. the singlet and triplet states in (1,1) configuration are nearly degenerate (see Fig. 7.4). Their measured splitting is usually on the order of micro-electron volt, whereas in our data $\Delta_2 = 0.25$ meV. Therefore, the second set of triangles in our data must correspond to another excited state. The possible candidates are the ordinary orbital states and the valley states unique to Si. One example with valley states is illustrated in Fig. 7.14, in which the singlet and triplet states are labeled with S and T, respectively and the two valley states are labeled with o and e. For negative bias as shown in Fig. 7.14(a), a second channel for electron transition through the singlet with e valley state can be accessible. The difference between S,e and S,o in (2,0) corresponds to Δ_1 while for (1,1) configuration it corresponds to Δ_2. For positive bias the spin blockade persists, as shown in Fig. 7.14(b).

In fact, calculation shows that when both spin and valley degrees of freedom are

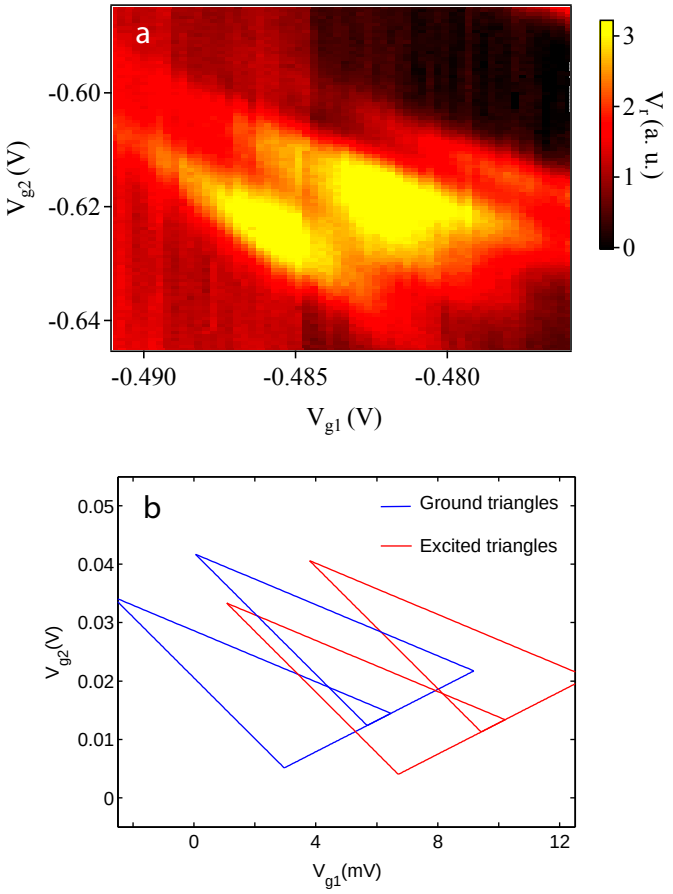

Figure 7.12: (a) The bias triangle data identical to Fig. 7.10. (b) The simulated triangles. The blue triangles are identical to the ones superimposed in Fig. 7.10 while for the red triangles the excitation energy of $\Delta_1 = 0.4$ mV and Δ_2=0.25 mV are included. In (b) the offset is chosen for clarity but the scales are the same as in (a).

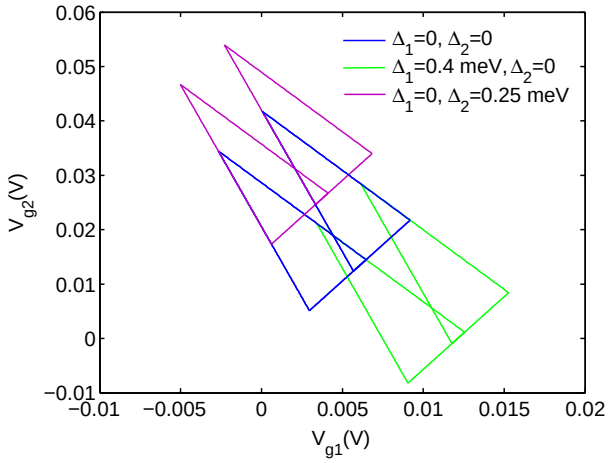

Figure 7.13: Simulated triangles demonstrating the individual effect of Δ_1 (green triangles) and Δ_2 (magenta triangles)

present, spin blockade involves many combinations of spin and valley states [83]. Regardless of the actual excited states involved, $\Delta_1 = 0.4$ meV and $\Delta_2 = 0.25$ meV are rather high energies. The fact that these transitions are visible demonstrates that the energy relaxation times in Si/SiGe DQDs are long.

7.4 Analysis of diode detector output

It is intriguing that Fig. 7.7, 7.10 and 7.11 strongly resemble transport measurements, even though they report charge sensing measurements. To understand this, we assume the transitions can be modeled as an RTS between two charge states labelled 0 and

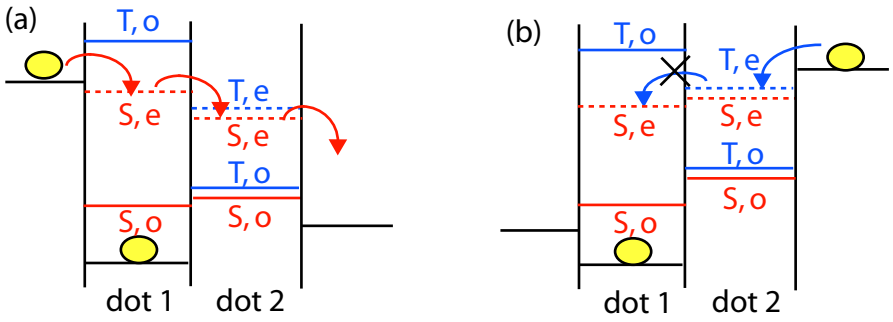

Figure 7.14: Schematic energy diagram of a DQD system with both spin and valley degrees of freedom. The valley states are labeled with o and e. The two valley states can provide two channels for singlet transitions, resulting in two pairs of bias triangles.

1 with power spectral density (PSD)[84, 85]

$$S(\omega) = \frac{4(\Delta I)^2}{(\tau_0 + \tau_1)[(1/\tau_0 + 1/\tau_1)^2 + \omega^2]} \tag{7.15}$$

where $\tau_{0,1}$ are the mean times spent in each state as in section 6.3.2. The amplitudes of states 0 and 1 are chosen to be 0 and ΔI respectively. The low-frequency plateau of $S(\omega)$ reaches a maximum when $\tau_0 = \tau_1$, which is when two states are degenerate in the DQD. We can express the signal entering the detector as $v(t) = v_0[1+x(t)]\cos\omega_0 t$. Here, $x(t) \ll 1$ is the fractional change in reflected voltage due to the RTS and its Fourier transform is $X(\omega)$. Assuming that the amplitude v_0 is also small, we can use the small-signal approximation [70] and Taylor expand the output current of the diode detector in powers of $v(t)$ as

$$i(v(t)) = v_0 G_d[1 + x(t)]\cos\omega_0 t + \frac{v_0^2}{2} G_d'[1 + x(t)]^2 \cos^2\omega_0 t + O(v_0^3), \tag{7.16}$$

G_d being the dynamic conductance of the diode and G'_d its first derivative with respect to the voltage [70]. G_d and G'_d are constants during the measurement. The Fourier transform of $i(t)$, ignoring high frequency (>15 Hz) terms and second order terms in $x(t)$, is

$$\tilde{i}(\omega) = \frac{v_0^2}{2} G'_d[\pi\delta(\omega) + X(\omega)]. \tag{7.17}$$

Now we can calculate the PSD $S_i(\omega)$ of the detector current using

$$S(\omega) = \lim_{T\to\infty} \frac{2|\tilde{i}(\omega)|^2}{T}. \tag{7.18}$$

The delta function associated with a dc background can be ignored. It can be seen that $\tilde{i}(\omega) \propto X(\omega)$ and subsequently $S_i(\omega) \propto S(\omega)$, where $S(\omega)$ is as in Eq. 7.15. Therefore, the signal is strongest when transitions occur either due to inter-dot tunneling within the DQD, or between one of the two dots and the bath.

Chapter 8

Future direction

We are starting to fabricate QDs in undoped Si/SiGe samples. It has been demonstrated that by removing the dopants, extremely stable QDs can be formed [9], enabling the measurement of T_2^* [22]. Without dopants, there will also be less dissipation for the rf resonant circuit, which can enhance the performance of the SET. A new kind of read-out method, replacing the tank circuit with a high-quality-factor microwave cavity at $f_0 \approx 5$ GHz, is being developed. The embedded SET will be operated in the supercurrent regime as a single Cooper pair transistor (SCPT) to further reduce any dissipation. The gate-tunable quantum inductance of the SCPT appears in parallel with the equivalent resonator circuit. Borrowing existing experimental results [86], the SCPT-induced shift in the resonant frequency is estimated to be

$$\frac{\partial \omega_0}{\partial n_g} \approx 2\pi \times 250\text{MHz}/e, \tag{8.1}$$

where n_g is the gate charge $n_g = C_g V_g/e$. The frequency pull corresponds to multiple linewidths of the cavity resonance and can significantly improve the charge sensitivity.

Bibliography

[1] R. Feynman, "Simulating physics with computers," International journal of theoretical physics **21**, 1572 (1982).

[2] D. Deutsch, "Quantum theory, the Church-Turing principle and the universal quantum computer," Proceedings of the Royal Society of London. Series A **400**, 97 (1985).

[3] P. Shor, "Algorithms for quantum computation: Discrete logarithms and factoring," Annual Symposium on Foundations of Computer Science pp. 124–134 (1994).

[4] L. Grover, "Quantum mechanics helps in searching for a needle in a haystack," Phys. Rev. Lett. **79**, 325 (1997).

[5] D. Loss and D. DiVincenzo, "Quantum computation with quantum dots," Physical Review A **57**, 120 (1998).

[6] D. M. Pozar, *Quantum Computation and Quantum Information* (Cambridge, 2007).

[7] C. B. Simmons, M. Thalakulam, N. Shaji, L. J. Klein, H. Qin, R. H. Blick, D. E. Savage, M. G. Lagally, S. N. Coppersmith, and M. A. Eriksson, "Single-electron

quantum dot in Si/SiGe with integrated charge sensing," Appl. Phys. Lett. **91**, 213103 (2007).

[8] E. P. Nordberg, G. A. T. Eyck, H. L. Stalford, R. P. Muller, R. W. Young, K. Eng, L. A. Tracy, K. D. Childs, J. R. Wendt, R. K. Grubbs, J. Stevens, M. P. Lilly, M. A. Eriksson, and M. S. Carroll, "Enhancement-mode double-top-gated metal-oxide-semiconductor nanostructures with tunable lateral geometry," Phys. Rev. B **80**, 115331 (2009).

[9] M. Borselli, K. Eng, E. Croke, B. Maune, B. Huang, R. Ross, A. Kiselev, P. Deelman, I. Alvarado-Rodriguez, A. Schmitz, *et al.*, "Pauli spin blockade in undoped Si/SiGe two-electron double quantum dots," Appl. Phys. Lett. **99**, 063109 (2011).

[10] W. H. Lim, C. H. Yang, F. A. Zwanenburg, and A. S. Dzurak, "Spin filling of valley-orbit states in a silicon quantum dot," Nanotechnology **22**, 335704 (2011).

[11] Y. S. Shin, R. Brunner, A. Shibatomi, T. Obata, T. Otsuka, J. Yoneda, Y. Shiraki, K. Sawano, Y. Tokura, Y. Harada, K. Ishibashi, and S. Tarucha, "Aluminum oxide for an effective gate in Si/SiGe two-dimensional electron gas systems," Semiconductor Science and Technology **26**, 055004 (2011).

[12] C. Payette, K. Wang, P. J. Koppinen, Y. Dovzhenko, J. C. Sturm, and J. R. Petta, "Single charge sensing and transport in double quantum dots fabricated from commercially grown Si/SiGe heterostructures," Appl. Phys. Lett. **100**, 043508 (2012).

[13] C. Tahan, M. Friesen, and R. Joynt, "Decoherence of electron spin qubits in Si-based quantum computers," Phys. Rev. B **66**, 035314 (2002).

[14] W. M. Witzel and S. D. Sarma, "Quantum theory for electron spin decoherence induced by nuclear spin dynamics in semiconductor quantum computer architectures: Spectral diffusion of localized electron spins in the nuclear solid-state environment," Phys. Rev. B **74**, 035322 (2006).

[15] G. Burkard, D. Loss, and D. P. DiVincenzo, "Coupled quantum dots as quantum gates," Phys. Rev. B **59**, 2070 (1999).

[16] W. A. Coish, J. Fischer, and D. Loss, "Exponential decay in a spin bath," Phys. Rev. B **77**, 125329 (2008).

[17] D. Loss and D. P. DiVincenzo, "Quantum computation with quantum dots," Phys. Rev. A **57**, 120 (1998).

[18] J. J. L. Morton, D. R. McCamey, M. A. Eriksson, and S. A. Lyon, "Embracing the quantum limit in silicon computing," Nature **479**, 345 (2011).

[19] A. Morello, J. J. Pla, F. A. Zwanenburg, K. W. Chan, K. Y. Tan, H. Huebl, M. Möttönen, C. D. Nugroho, C. Yang, J. A. van Donkelaar, A. D. C. Alves, D. N. Jamieson, C. C. Escott, L. C. L. Hollenberg, R. G. Clark, and A. S. Dzurak, "Single-shot readout of an electron spin in silicon," Nature **467**, 687 (2010).

[20] C. B. Simmons, J. R. Prance, B. J. van Bael, T. S. Koh, Z. Shi, D. E. Savage, M. G. Lagally, R. Joynt, M. Friesen, S. N. Coppersmith, and M. A. Eriksson, "Tunable Spin Loading and T1 of a Silicon Spin Qubit Measured by Single-Shot Readout," Phys. Rev. Lett. **106**, 156804 (2011).

[21] J. R. Prance, Z. Shi, C. B. Simmons, D. E. Savage, M. G. Lagally, L. R. Schreiber, L. M. K. Vandersypen, M. Friesen, R. Joynt, S. N. Coppersmith, and M. A.

Eriksson, "Single-Shot Measurement of Triplet-Singlet Relaxation in a Si/SiGe Double Quantum Dot," Phys. Rev. Lett. **108**, 046808 (2012).

[22] B. M. Maune, M. G. Borselli, B. Huang, T. D. Ladd, P. W. Deelman, K. S. Holabird, A. A. Kiselev, I. Alvarado-Rodriguez, R. S. Ross, A. E. Schmitz, M. Sokolich, C. A. Watson, M. F. Gyure, and A. T. Hunter, "Coherent singlet-triplet oscillations in a silicon-based double quantum dot," Nature **481**, 344 (2012).

[23] H. Bluhm, S. Foletti, I. Neder, M. Rudner, D. Mahalu, V. Umansky, and A. Yacoby, "Dephasing time of GaAs electron-spin qubits coupled to a nuclear bath exceeding 200 μs," Nat. Phys. **7**, 109 (2011).

[24] J. M. Elzerman, R. Hanson, L. H. W. van Beveren, B. Witkamp, L. M. K. Vandersypen, and L. P. Kouwenhoven, "Single-shot read-out of an individual electron spin in a quantum dot," Nature **430**, 431 (2004).

[25] J. R. Petta, A. C. Johnson, J. M. Taylor, E. A. Laird, A. Yacoby, M. D. Lukin, C. M. Marcus, M. P. Hanson, and A. C. Gossard, "Coherent manipulation of coupled electron spins in semiconductor quantum dots," Science **309**, 2180 (2005).

[26] F. H. L. Koppens, K. C. Nowack, and L. M. K. Vandersypen, "Spin Echo of a Single Electron Spin in a Quantum Dot," Phys. Rev. Lett. **100**, 236802 (2008).

[27] J. R. Petta, A. C. Johnson, A. Yacoby, C. M. Marcus, M. P. Hanson, and A. C. Gossard, "Pulsed-gate measurements of the singlet-triplet relaxation time in a two-electron double quantum dot," Phys. Rev. B **72**, 161301 (2005).

[28] R. People, J. C. Bean, D. V. Lang, A. M. Sergent, H. L. Strmer, K. W. Wecht, R. T. Lynch, and K. Baldwin, "Modulation doping in Ge_xSi_{1-x}/Si strained layer heterostructures," Appl. Phys. Lett **45**, 1231 (1984).

[29] H. Jorke and H. J. Herzog, "Mobility enhancement in modulation doped Si-$Si_{1-x}Ge_x$ superlattice grown by molecular beam epitaxy," Proc. 1st Int. Symp. on Silicon MBE **85-7**, 194 (1985).

[30] G. Abstreiter, H. Brugger, T. Wolf, H. Jorke, and H. J. Herzog, "Strain-Induced Two-Dimensional Electron Gas in Selectively Doped Si/Si_xGe_{1-x} Superlattices," Phys. Rev. Lett. **54**, 2441 (1985).

[31] D. Paul, "Si/SiGe heterostructures: from material and physics to devices and circuits," Semiconductor Science and Technology **19**, R75 (2004).

[32] L. J. Klein, K. A. Slinker, J. L. Truitt, S. Goswami, K. L. M. Lewis, S. N. Coppersmith, D. W. van der Weide, M. Friesen, R. H. Blick, D. E. Savage, M. G. Lagally, C. Tahan, R. Joynt, M. A. Eriksson, J. O. Chu, J. A. Ott, and P. M. Mooney, "Coulomb blockade in a silicon/silicongermanium two-dimensional electron gas quantum dot," Appl. Phys. Lett. **84**, 4047 (2004).

[33] C. B. Simmons, M. Thalakulam, B. M. Rosemeyer, B. J. van Bael, E. K. Sackmann, D. E. Savage, M. G. Lagally, R. Joynt, M. Friesen, S. N. Coppersmith, and M. A. Eriksson, "Charge sensing and controllable tunnel coupling in a Si/SiGe double quantum dot," Nano Lett. **9**, 3234 (2009).

[34] A. Shnirman and G. Schön, "Quantum measurements performed with a single-electron transistor," Phys. Rev. B **57**, 15400 (1998).

[35] M. Field, C. G. Smith, M. Pepper, D. A. Ritchie, J. E. F. Frost, G. A. C. Jones, and D. G. Hasko, "Measurements of Coulomb blockade with a noninvasive voltage probe," Phys. Rev. Lett. **70**, 1311 (1993).

[36] S. J. Angus, A. J. Ferguson, A. S. Dzurak, and R. G. Clark, "A silicon radio-frequency single electron transistor," Appl. Phys. Lett. **92**, 112103 (2008).

[37] R. J. Schoelkopf, P. Wahlgren, A. A. Kozhevnikov, P. Delsing, and D. E. Prober, "The radio-frequency single-electron transistor (RF-SET): a fast and ultrasensitive electrometer," Science **280**, 1238 (1998).

[38] W. Lu, Z. Ji, L. Pfeiffer, K. W. West, and A. J. Rimberg, "Real-time detection of electron tunnelling in a quantum dot," Nature **423**, 422 (2003).

[39] H. Brenning, S. Kafanov, T. Duty, S. Kubatkin, and P. Delsing, "An ultrasensitive radio-frequency single-electron transistor working up to 4.2 K," J. Appl. Phys. **100**, 114321 (2006).

[40] W. W. Xue, Z. Ji, F. Pan, J. Stettenheim, M. P. Blencowe, and A. J. Rimberg, "Measurement of quantum noise in a single-electron transistor near the quantum limit," Nat. Phys. **5**, 660 (2009).

[41] D. K. Ferry and S. M. Goodnick, *Transport in Nanostructures* (Cambridge University Press, 1997).

[42] A. C. Johnson, *Charge Sensing and Spin Dynamics in GaAs Quantum Dots*, Ph.D. thesis, Harvard University (2005).

[43] D. Goldhaber-Gordon, H. Shtrikman, D. Mahalu, D. Abusch-Magder, U. Meirav, and M. A. Kastner, "Kondo effect in a single-electron transistor," Nature **391**, 156 (1998).

[44] S. M. Cronenwett, T. H. Oosterkamp, and L. P. Kouwenhoven, "A Tunable Kondo Effect in Quantum Dots," Science **281**, 540 (1998).

[45] Y. Meir, N. S. Wingreen, and P. A. Lee, "Low-temperature transport through a quantum dot: The Anderson model out of equilibrium," Phys. Rev. Lett. **70**, 2601 (1993).

[46] P. W. Anderson, "Localized Magnetic States in Metals," Phys. Rev. **124**, 41 (1961).

[47] A. Vidan, M. Stopa, R. M. Westervelt, M. Hanson, and A. C. Gossard, "Multi-peak Kondo Effect in One- and Two-Electron Quantum Dots," Phys. Rev. Lett. **96**, 156802 (2006).

[48] S. Sasaki, S. D. Franceschi, J. M. Elzerman, W. G. van der Wiel, S. T. M. Eto, and L. P. Kouwenhoven, "Kondo effect in an integer-spin quantum dot," Nature **405**, 764 (2000).

[49] W. G. van der Wiel, S. De Franceschi, J. M. Elzerman, S. Tarucha, L. P. Kouwenhoven, J. Motohisa, F. Nakajima, and T. Fukui, "Two-Stage Kondo Effect in a Quantum Dot at a High Magnetic Field," Phys. Rev. Lett. **88**, 126803 (2002).

[50] A. Kogan, G. Granger, M. A. Kastner, D. Goldhaber-Gordon, and H. Shtrikman, "Singlet-triplet transition in a single-electron transistor at zero magnetic field," Phys. Rev. B **67**, 113309 (2003).

[51] G. Granger, M. A. Kastner, I. Radu, M. P. Hanson, and A. C. Gossard, "Two-stage Kondo effect in a four-electron artificial atom," Phys. Rev. B **72**, 165309 (2005).

[52] M. Pustilnik and L. I. Glazman, "Kondo Effect in Real Quantum Dots," Phys. Rev. Lett. **87**, 216601 (2001).

[53] M. Pustilnik, L. I. Glazman, and W. Hofstetter, "Singlet-triplet transition in a lateral quantum dot," Phys. Rev. B **68**, 161303 (2003).

[54] A. Posazhennikova, B. Bayani, and P. Coleman, "Conductance of a spin-1 quantum dot: The two-stage Kondo effect," Phys. Rev. B **75**, 245329 (2007).

[55] T. B. Boykin, G. Klimeck, M. A. Eriksson, M. Friesen, S. N. Coppersmith, P. von Allmen, F. Oyafuso, and S. Lee, "Valley splitting in strained silicon quantum wells," Appl. Phys. Lett. **84**, 115 (2004).

[56] S. Goswami, K. A. Slinker, M. Friesen, L. M. McGuire, J. L. Truitt, C. Tahan, L. J. Klein, J. O. Chu, P. M. Mooney, D. W. van der Weide, R. Joynt, S. N. Coppersmith, and M. A. Eriksson, "Controllable valley splitting in silicon quantum devices," Nat. Phys. **3**, 41 (2007).

[57] L. J. Klein, D. E. Savage, and M. A. Eriksson, "Coulomb blockade and Kondo effect in a few-electron silicon/silicon-germanium quantum dot," Appl. Phys. Lett **90**, 033103 (2007).

[58] G. P. Lansbergen, G. C. Tettamanzi, J. Verduijn, N. Collaert, S. Biesemans, M. Blaauboer, and S. Rogge, "Tunable Kondo effect in a single donor atom," nano lett. **10**, 455 (2010).

[59] G. C. Tettamanzi, J. Verduijn, G. P. Lansbergen, M. Blaauboer, M. J. Calderón, R. Aguado, and S. Rogge, "Magnetic-Field Probing of an SU(4) Kondo Resonance in a Single-Atom Transistor," Phys. Rev. Lett. **108**, 046803 (2012).

[60] S.-y. Shiau, S. Chutia, and R. Joynt, "Valley Kondo effect in silicon quantum dots," Phys. Rev. B **75**, 195345 (2007).

[61] S.-y. Shiau and R. Joynt, "Spin-valley Kondo effect in multielectron Si quantum dots," Phys. Rev. B **76**, 205314 (2007).

[62] P. Jarillo-Herrero, J. Kong, H. S. J. van der Zant, C. Dekker, L. P. Kouwenhoven, and S. D. Franceschi, "Orbital Kondo effect in carbon nanotubes," Nature **434**, 484 (2005).

[63] S. De Franceschi, S. Sasaki, J. M. Elzerman, W. G. van der Wiel, S. Tarucha, and L. P. Kouwenhoven, "Electron Cotunneling in a Semiconductor Quantum Dot," Phys. Rev. Lett. **86**, 878 (2001).

[64] M. Friesen and S. N. Coppersmith, "Theory of valley-orbit coupling in a Si/SiGe quantum dot," Phys. Rev. B **81**, 115324 (2010).

[65] D. Culcer, X. Hu, and S. Das Sarma, "Interface roughness, valley-orbit coupling, and valley manipulation in quantum dots," Phys. Rev. B **82**, 205315 (2010).

[66] T. A. Fulton and G. J. Dolan, "Observation of single-electron charging effects in small tunnel junctions," Phys. Rev. Lett. **59**, 109 (1987).

[67] T. A. Fulton, P. L. Gammel, D. J. Bishop, L. N. Dunkleberger, and G. J. Dolan, "Observation of combined Josephson and charging effects in small tunnel junction circuits," Phys. Rev. Lett. **63**, 1307 (1989).

[68] M. P. Blencowe, J. Imbers, and A. D. Armour, "Dynamics of a nanomechanical resonator coupled to a superconducting single-electron transistor," New J. Phys. **7**, 236 (2005).

[69] Z. Ji, *Towards the Quantum Limit: A Single Electron Transistor Analysis*, Ph.D. thesis, Rice University (2008).

[70] M. A. Nielsen and I. L. Chuang, *Microwave Engineering* (Wiley, 1997).

[71] T. Fujisawa and Y. Hirayama, "Charge noise analysis of an AlGaAs/GaAs quantum dot using transmission-type radio-frequency single-electron transistor technique," Appl. Phys. Lett. **77**, 543 (2000).

[72] W. G. van der Wiel, S. De Franceschi, J. M. Elzerman, T. Fujisawa, S. Tarucha, and L. P. Kouwenhoven, "Electron transport through double quantum dots," Rev. Mod. Phys. **75**, 1 (2002).

[73] K. Ono, D. G. Austing, Y. Tkura, and S. Tarucha, "Current Rectification by Pauli Exclusion in a Weakly Coupled Double Quantum Dot System," Science **297**, 1313 (2002).

[74] A. K. Hüttel, H. Qin, A. W. Holleitner, R. H. Blick, K. Neumaier, D. Weinmann, K. Eberl, and J. P. Kotthaus, "Spin blockade in ground-state resonance of a quantum dot," europhys. lett. **62**, 712 (2003).

[75] L. P. Rokhinson, L. J. Guo, S. Y. Chou, and D. C. Tsui, "Spin transitions in a small Si quantum dot," Phys. Rev. B **63**, 035321 (2001).

[76] F. H. L. Koppens, J. A. Folk, J. M. Elzerman, R. Hanson1, L. H. W. van Beveren, I. T. Vink, H. P. Tranitz, W. Wegscheider, L. P. Kouwenhoven, and L. M. K.

Vandersypen, "Control and detection of singlet-triplet mixing in a random nuclear field," Science **309**, 1346 (2005).

[77] A. C. Johnson, J. R. Petta, C. M. Marcus, M. P. Hanson, and A. C. Gossard, "Singlet-triplet spin blockade and charge sensing in a few-electron double quantum dot," Phys. Rev. B **72**, 165308 (2005).

[78] H. W. Liu, T. Fujisawa, Y. Ono, H. Inokawa, A. Fujiwara, K. Takashina, and Y. Hirayama, "Pauli-spin-blockade transport through a silicon double quantum dot," Phys. Rev. B **77**, 073310 (2008).

[79] N. Shaji, C. B. Simmons, M. Thalakulam, L. J. Klein, H. Qin, H. Luo, D. E. Savage, M. G. Lagally, A. J. Rimberg, R. Joynt, M. Friesen, R. H. Blick, S. N. Coppersmith, and M. A. Eriksson, "Spin blockade and lifetime-enhanced transport in a few-electron Si/SiGe double quantum dot," Nat. Phys. **4**, 540 (2008).

[80] C. B. Simmons, T. S. Koh, N. Shaji, M. Thalakulam, L. J. Klein, H. Qin, H. Luo, D. E. Savage, M. G. Lagally, A. J. Rimberg, R. Joynt, R. Blick, M. Friesen, S. N. Coppersmith, and M. A. Eriksson, "Pauli spin blockade and lifetime-enhanced transport in a Si/SiGe double quantum dot," Phys. Rev. B **82**, 245312 (2010).

[81] N. W. Ashcroft and N. D. Mermin, *Solid State Physics* (Brooks/Cole, 1976).

[82] C. B. Simmons, T. S. Koh, N. Shaji, M. Thalakulam, L. J. Klein, H. Qin, H. Luo, D. E. Savage, M. G. Lagally, A. J. Rimberg, R. Joynt, R. Blick, M. Friesen, S. N. Coppersmith, and M. A. Eriksson, "Pauli spin blockade and lifetime-enhanced transport in a Si/SiGe double quantum dot," Phys. Rev. B **82**, 245312 (2010).

[83] N. Rohling and G. Burkard, "Universal quantum computing with spin and valley states," New Journal of Physics **14**, 083008 (2012).

[84] S. Machlup, "Noise in Semiconductors: Spectrum of a Two Parameter Random Signal," J. Appl. Phys **25**, 341 (1953).

[85] M. J. Kirton and M. J. Uren, "Noise in solid-state microstructures: A new perspective on individual defects, interface states and low-frequency (1/f) noise," Adv. Phys **38**, 367 (1989).

[86] M. Sillanpää, *Quantum Device Applications of Mesoscopic Superconductivity*, Ph.D. thesis, Helsinki University of Technology (2005).